Spreading Behavior of Molten Metal Microdroplets

by

Ho-Young Kim

B. S., Mechanical Engineering, Seoul National University (1994)

S. M., Mechanical Engineering, Massachusetts Institute of Technology (1996)

Submitted to the Department of Mechanical Engineering
in Partial Fulfillment of the Requirements for the Degree of

DOCTOR OF PHILOSOPHY IN MECHANICAL ENGINEERING

at the

MASSACHUSETTS INSTITUTE OF TECHNOLOGY

February 1999

Signature of Author: _____
Department of Mechanical Engineering
February, 1999

Certified by: _____
Jung-Hoon Chun
Associate Professor of Mechanical Engineering
Chairman, Doctoral Thesis Committee

Accepted by: _____
Ain A. Sonin
Professor of Mechanical Engineering
Chairman, Department Graduate Committee

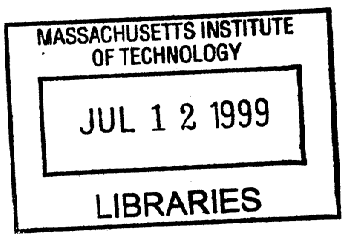

Spreading Behavior of Molten Metal Microdroplets

by

Ho-Young Kim

Submitted to the Department of Mechanical Engineering
on December 15, 1998 in Partial Fulfillment of the Requirements for the Degree of
Doctor of Philosophy in Mechanical Engineering

ABSTRACT

Deposition of molten microdroplets is fundamental to many emerging droplet-based manufacturing (DBM) processes. Although the spreading behavior of ordinary liquid and molten droplets has been studied extensively for years, some basic questions remain unanswered. Specifically, the fundamental mechanisms of abnormal spreading behavior, such as splashing and bouncing, have yet to be satisfactorily addressed. An understanding of these mechanisms is essential to determine the optimal deposition conditions for the DBM process. This thesis investigates the fundamental, but poorly understood, behavior of liquid and molten metal droplets upon impact on solid surfaces.

The splashing of liquid droplets is addressed first. A linear perturbation theory is developed for the interface instabilities of a radially-expanding, liquid sheet in cylindrical geometries. The theory is then applied to rapidly spreading droplets as the fundamental mechanism behind splashing. The effects of such factors as the transient profile of the interface radius, the perturbation onset time, and the Weber number on the analysis results are examined. The analysis shows that the wave number of maximum instability does not remain constant but rather, changes during spreading because of time-dependent coefficients in the amplitude equation. A large impact inertia, associated with a high Weber number, promotes interface instability and prefers high wave number for maximum instability.

The next stage investigates the oscillations of liquid droplets upon collision with solid surfaces as a prerequisite for understanding droplet bouncing. Experiments using a high speed video system show that the droplets with higher impact inertia oscillate more vigorously upon collision. The oscillation is strongly affected by the wetting between the liquid droplet and the solid surface, such that the oscillation is greatly promoted in poor wetting conditions. In addition, this thesis develops approximate models based on the variational principle, rather than the Navier-Stokes equation to simulate the droplet oscillation. The results of the models are in good agreement with the experimental data. The analysis shows that the relative magnitudes of surface energy and viscous dissipation play critical roles in determining droplet dynamics.

Following the oscillation study, the bouncing of molten metal droplets upon collision with subcooled target surfaces is studied. To determine the conditions for bouncing and sticking, an empirical regime map is constructed using an approximate model and extensive experimental data. A clear trend develops, illustrating that bouncing occurs when solidification is slow compared to oscillation, when a molten metal droplet collides with a nonwetting surface. It is also found that bouncing is prohibited by good wetting between the droplet and the target, which suggests that the wetting be an additional parameter affecting the bouncing behavior.

Thesis Supervisor: Dr. Jung-Hoon Chun
Title: Associate Professor of Mechanical Engineering

Acknowledgments

I would like to thank Prof. Jung-Hoon Chun for guiding and supporting my research with consistent trust and encouragement. My sincere appreciation goes to the members of my thesis committee, Prof. Frank Feng and Prof. Taiqing Qiu. It was a great experience and pleasure to discuss and learn about hydrodynamic stability with Prof. Feng. Prof. Qiu introduced to me the new world of microelectromechanical systems and showed an exemplary attitude to explore new physical phenomena. I would also like to thank Prof. Ain Sonin and Dr. Nannaji Saka for their valuable advice on my research.

It has been a great pleasure to work with the friends at the Droplet-Based Manufacturing laboratory. Thank you, Dr. Chen-An Chen, who was indeed a friend in my hard time. Jeanie Cherng was kind and considerate enough to offer me so much help and to be a sounding wall for over 4 years. Dr. Sukyoung Chey's warm care and spiritual help kept me sane at MIT. Jiun-Yu Lai was always ready to give help and was such a pleasant friend to talk with about any matters. A good nature and sincerity of Juan-Carlos Rocha are not forgettable with a glass of tequila at Revere Beach.

With the warmest regard and appreciation to my friends who supported me in so many ways. Very special thanks to Jennifer Shin, without whose help this thesis would not have been possible. Friends I met at MIT, especially Woosok Chang, Taewoong Koo, Hyuksang Kwon, Dr. Daeyup Lee, Youngchul Ra, Sokwoo Rhee, Steve Rhee, and Dr. James Jangsik Shin, all deserve my sincere gratitude.

My thanks go to Ms. Leslie Regan and Ms. Lisa Falco for their excellent administrative assistance and for patiently waiting for this thesis to be finalized.

Finally, last but not least, I would like to acknowledge my parents with my greatest thanks. I am grateful to my sister and brothers for their unconditional love and support.

Table of Contents

List of Tables

List of Figures

CHAPTER 1

INTRODUCTION

1.1. General background

The deposition of molten metal droplets plays an important role in many emerging fields of technology, such as spray forming, spray coating, rapid prototyping, and electronic packaging. Deposition phenomena comprise the impact of individual droplets on substrates, coalescence of adjacent splats after impact, bonding between droplets and deposit, and microstructural evolution of a sprayed deposit. The impact and spreading behavior of each droplet are crucial to the overall deposition process, for they govern the subsequent processes. Accurate understanding and control of droplet deposition is essential since it determines geometric definition, such as surface porosity and conformity to the target shapes, and mechanical properties of deposit. Although extensive research on the spreading behavior of molten metal droplets has been performed so far (Madejski 1976; McPherson 1981; Liu et al. 1995; Pasandideh-Fard et al. 1998; Xiong et al. 1998), complicated physical phenomena involved in the subject have rendered serious difficulties in understanding the problem. The difficulties mainly arise from the inherently coupled nature of fluid motion and cooling.

Describing the motion of a spreading droplet requires solving the moving boundary problem for the Navier-Stokes equation. Furthermore, the contact between a liquid droplet and a solid surface demands consideration of the physics of wetting, of which complete understanding is still beyond our ability (de Gennes 1985). The spreading behavior of ordinary liquid droplets without solidification has been studied extensively for many years (Worthington 1877a,b; Engel 1955; Bechtel et al. 1981; Stow and Hadfield 1981; Chandra and Avedisian 1991; Pasandideh-Fard et al. 1996). Regardless of the degree of solidification during spreading, fluid motion is fundamental to understanding molten metal impact behavior. Moreover, at the limit at which solidification is much slower than fluid motion, the treatment of molten metal droplets is identical to that of ordinary liquid droplets (Trapaga and Szekely 1991; Bennett and Poulikakos 1993).

Nonetheless, the description of dynamics of molten metal droplets deposited on subcooled (colder than the melting point of the droplet material) target surfaces involves solidification in addition to fluid motion. Madejski (1976) and Solonenko et al. (1994)

have taken approximate but analytical approaches to the simultaneous effects of solidification and fluid flow in spreading droplets. However, the majority of past modeling efforts employed computational methods due to the complexity of the phenomenon. The full Navier-Stokes equation and the Stefan problem of solidification were simultaneously solved by Liu et al. (1993), San Marchi et al. (1993), and Liu et al. (1994). Trapaga et al. (1992), Waldvogel and Poulikakos (1997), and Pasandideh-Fard et al. (1998) solved the two-dimensional energy equation, instead of the Stefan problem, with the Navier-Stokes equation. In addition to modeling, experimental studies were carried out on the behavior of impacting molten droplets (Inada 1988; Watanabe et al. 1992; Inada and Yang 1994; Schiaffino 1996). The experiments showed that although the effects of solidification are negligible in the initial stages of rapid spreading, in the later stages, solidification arrests the fringe of the impacting droplet and interacts with the droplet oscillations.

1.2. Scope of the present investigation

In most spray-deposition processes, it is desired to achieve the deposition of droplets in a controlled and precise manner. Therefore, the mechanisms behind abnormal impact behavior such as splashing and bouncing must be understood to produce high-quality deposits. Splashing increases the bulk and surface porosity of a deposit and consequently deteriorates its quality. A high degree of splashing degrades the sticking efficiency of the spray-deposition process, decreasing process yield. It is highly likely that droplets which tend to oscillate vigorously have poor contact with the substrate, which hinders rapid solidification. In addition, the deposition of an individual molten microdroplet for the electronic packaging demands a thorough understanding of droplet oscillations to both prevent droplet bouncing and predict final bump shape.

We obtain the independent parameters which affect the spreading behavior of droplets by dimensional analysis. In the case of isothermal deposition, neglecting gravity effects, we find the following relevant scaling parameters: Weber number, Ohnesorge number, and additional parameter(s) determined by the interfacial phenomena between the droplet liquid and target solid. The Weber number, We, is the ratio of inertial to surface tension forces at impact, and the Ohnesorge number, Oh, is the ratio of viscous to surface tension forces. We assume that only the equilibrium contact angle, θ, plays the dominant role as the interfacial parameter. The Weber number scales the driving force for the droplet spreading, and the Ohnesorge number scales the force that resists the

spreading (Schiaffino 1996). Schiaffino derived four different, asymptotic spreading regimes given good wetting conditions.

Most spray-deposition applications operate in the regime of inviscid, impact-driven spreading, where We >> 1 and Oh << $We^{1/2}$. The regime is characterized by rapid initial spreading followed by well-pronounced oscillations. We can subdivide this regime based on the strength of the spreading and the oscillations. When the driving force of the spreading is very strong, the droplet develops an unstable spreading front which leads to splashing. When the oscillations are very strong, the droplet may disengage from the target surface, which is referred to as bouncing, or disintegrate, which is called necking, during recoiling.

This thesis investigates the droplet dynamics in the regime of inviscid, impact-driven spreading. We study the initial spreading stages that possess excessive driving force to understand the splashing phenomenon. We then investigate the subsequent oscillation phenomena. In this study, the effects of the contact angle as well as Weber number and Ohnesorge number are investigated since wetting plays an important role in the oscillation stages. After describing the oscillation dynamics, we study the bouncing of molten metal droplets as an extremely violent form of droplet oscillation. We include the effects of solidification in the study to explain the strong dependency of bouncing and sticking behavior on thermal conditions.

1.3. Organization of thesis

The present chapter describes the background and scope of the thesis. Chapter 2 studies the splashing phenomena of liquid droplets. Although splashing of liquid droplets upon collision with solid surfaces is frequently observed in a variety of situations, its fundamental mechanism is still not fully understood. The linear perturbation theory is developed to model the unstable spreading front of a radially expanding liquid sheet which emerges from a droplet upon collision with a solid surface. Chapter 3 describes the oscillation dynamics of various liquid droplets on different solid surfaces. We experimentally identify the effects of impact and surface conditions on spreading and subsequent oscillations. The experimental data are compared with approximate models. The bouncing of molten metal droplets upon colliding with subcooled targets is investigated in Chapter 4. The regime map for the bouncing and sticking of molten metal droplets is constructed based on experimental results and modeling. Chapter 5 offers the conclusions of this thesis.

CHAPTER 2

SPLASHING OF LIQUID DROPLETS UPON COLLISION WITH SOLID SURFACES

2.1. Introduction

A droplet with large inertia frequently spreads with fingers extending from the edge when it impinges on a solid surface. Although the behavior of a spreading droplet after colliding with a target plane has been the subject of intense study for many years (Worthington 1877a,b; Engel 1955; Harlow and Shannon 1967; Bowden and Field 1964; Chandra and Avedisian 1991; Fukai et al. 1995), comparatively less work has been done on a splashing droplet – a droplet that develops an unstable periphery. Levin and Hobbs (1971) observed the formation of a crown, i.e., the detachment of a watersheet from a target surface, when a water drop impinges on a copper hemisphere. Stow and Hadfield (1981) photographed the early development of a watersheet emerging from the drop/target contact area, and were able to distinguish splashing droplets from non-splashing ones by the release of an unstable watersheet in the very early stages of spreading. Mundo et al. (1995) characterized the size and velocity of the secondary droplets produced from a droplet colliding with a rotating disc at an angle. Thoroddsen and Sakakibara (1998) first performed a systematic study on the evolution of the fingers developing from a droplet interface spreading on a flat glass substrate. Furthermore, recent experiments (Thoroddsen and Sakakibara 1998; Marmanis and Thoroddsen 1996) showed that the unstable azimuthal undulation is a characteristic feature of splashing. For this reason, we consider splashing to be the unstable expansion of the spreading front in colliding droplets, including crown formation as an extreme case of splashing.

Significant experimental observations of splashing droplets are summarized as the following: (1) Splashing manifests itself in the very early stages of spreading. (Stow and Hadfield 1981; Thoroddsen and Sakakibara 1998) (2) Splashing occurs when the impacting droplet has significant kinetic energy as compared to surface energy and it is promoted by rough target surfaces (Stow and Hadfield 1981; Mundo et al. 1995) A crown even develops under severe destabilizing conditions. (3) Increasing the impact inertia increases the number of fingers (Marmanis and Thoroddsen 1996), and this number does not change significantly during spreading (Thoroddsen and Sakakibara 1998).

A few articles (Allen 1975; Mundo et al. 1995; Thoroddsen and Sakakibara 1998) have addressed the origin of splashing, but the basic mechanism of splashing is still far from clear. Allen (1975) suggested that a radially decelerating interface of a spreading droplet be Rayleigh-Taylor unstable and calculated the most dangerous wavelength based on the average deceleration required to bring the spreading to a halt. He modeled the radially extending flow into one-directional plane motion and assumed that the deceleration was due to viscous damping. However, his model overlooks the effects of a changing interface length during spreading and the effect of curvature on the instabilities. In addition, the selection of the representative deceleration is somewhat arbitrary. Mundo et al. (1995) suggested that the crown develop when the total energy of a droplet prior to impact exceeds the amount of energy dissipated by viscosity during spreading. On the other hand, Thoroddsen and Sakakibara (1998) contended that the fingering is due to the Rayleigh-Taylor instability of the decelerating fluid ring at the droplet bottom before hitting a target.

To elucidate the fundamental mechanism behind splashing we note that the behavior of a liquid sheet released upon impact is crucial in understanding splashing. In the present work, we study the Rayleigh-Taylor instability of a radially expanding sheet, in "cylindrical" geometry, as a major mechanism of splashing. Figure 2.1 shows a sheet that is typically released during impact-driven spreading.

Although the Rayleigh-Taylor instability has been extensively studied for many years, most of effort has been focused on the plane (Taylor 1950; Menikoff et al. 1978; Tryggvason 1988; Berning and Rubenchik 1998) and spherical geometries (Plesset 1954; Plesset and Mitchell 1956; Birkhoff 1956; Baker et al. 1984). Especially, interests in cavitation bubbles, pulsations of underwater explosion bubbles, and sonoluminescence (Hilgenfeldt et al. 1998) have brought attention to the dynamics of spherical bubbles. Behavior of a gas bubble in an incompressible liquid under adiabatic or isothermal conditions is described by the Rayleigh-Plesset (RP) equation (Plesset and Prosperetti 1977; Feng and Leal 1997). The distortion amplitude of the spherical interface is governed by an equation whose coefficients are time-dependent as ruled by the RP equation. When the amplitude of the radial oscillation is small, the governing equations for the shape modes are reduced to Mathieu's equation. On the other hand, Brenner et al. (1995) examined both the Rayleigh-Taylor and the parametric instability mechanisms for a large amplitude case. Generally, numerical methods are required to understand such a case.

In the present work, we investigate the instabilities of a radially-expanding circular interface in cylindrical geometries. While the bubble dynamics are governed by

the RP equation, the motion of the liquid sheet of our interest is ruled by the dynamics of droplet spreading. Since the details of initial droplet spreading stages are not precisely known, we build a simple model on the expansion of a liquid sheet upon impact. It is assumed that the deceleration of the sheet interface is due to a mass-conservation controlled flow characteristic rather than viscous damping. An equation governing the azimuthal instability of an expanding sheet is obtained using domain perturbation methods. The dynamic conditions of a droplet prior to impact are represented by the Weber number in our analysis. Numerical simulation investigates the sensitivity of the instability analysis to the modeling assumptions and the role of impact conditions.

2.2. Derivation of the amplitude equation

Consider a radially-expanding liquid sheet whose expansion rate, i.e., radial velocity as a function of time, is known *a priori*. Stability of the edge of the two-dimensional, liquid sheet subjected to an azimuthal disturbance is investigated. Without disturbance, its shape is given only by time, and the velocity is determined merely by time and radial distance. However, under the azimuthal disturbance the location of the periphery is dependent upon an azimuthal angle θ as well as time as shown in Figure 2.2.

We nondimensionalize the flow parameters based on the characteristic radius R_D^* and the characteristic velocity U^*. In the case of rapidly spreading liquid droplets, R_D^* and U^* correspond to the original droplet radius before impact and the impact velocity, respectively. The characteristic time scale τ^* is given by $\tau^* = R_D^*/U^*$, and the velocity potential is scaled by $R_D^* U^*$. The following quantities are all nondimensionalized based on, R_D^*, U^*, τ^*, and $R_D^* U^*$, and their forms are shown in Appendix A.

The velocity potential of the liquid ϕ is defined such that the radial velocity v_r and the azimuthal velocity v_θ satisfy, respectively,

$$v_r = \frac{\partial \phi}{\partial r}, \tag{2.1}$$

and

$$v_\theta = \frac{1}{r}\frac{\partial \phi}{\partial \theta}. \tag{2.2}$$

It is supposed that the velocity potential and the outer radius of the fluid R are slightly disturbed, so that they are expressed as

$$\phi = \phi_0(t,r) + \phi_1(t,r,\theta), \tag{2.3}$$

and

$$R = R_0(t) + R_1(t,\theta), \tag{2.4}$$

where ϕ_0 and R_0 denote the base or axisymmetric spreading solutions and ϕ_1 and R_1 are small perturbations. We neglect the effect of viscosity, hence the governing equation for incompressible and irrotational flow is

$$\nabla^2 \phi = 0. \tag{2.5}$$

We model the axisymmetric liquid expansion by a line source at the center, giving the base flow solution as

$$\phi_0 = M(t) \ln r, \tag{2.6}$$

where M is the strength of the source. Then the base solution of the radial velocity is expressed as

$$\frac{\partial \phi_0}{\partial r} = \frac{M}{r}, \tag{2.7}$$

The kinematic boundary condition (KBC) at the edge of the expanding fluid is

$$\frac{\partial \phi}{\partial r} = \frac{\partial R}{\partial t} + \frac{1}{r^2}\frac{\partial \phi}{\partial \theta}\frac{\partial R}{\partial \theta}. \tag{2.8}$$

Using Eqs. (2.3) and (2.4), we rewrite KBC as

$$\frac{\partial \phi_0}{\partial r} + \frac{\partial \phi_1}{\partial r} = \frac{\partial R_0}{\partial t} + \frac{\partial R_1}{\partial t} + \frac{1}{r^2}\frac{\partial \phi_1}{\partial \theta}\frac{\partial R_1}{\partial \theta}. \tag{2.9}$$

It is noted that KBC is imposed on a moving interface at $r = R_0 + R_1$, whose location is not known *a priori*. Therefore, the domain perturbation method is applied to find a boundary condition which is to be imposed on an unperturbed interface. From the Taylor series expansion, we obtain the following expressions which are correct to the first order:

$$\left.\frac{\partial \phi_0}{\partial r}\right)_{r=R_0+R_1} \approx \left.\frac{\partial \phi_0}{\partial r}\right)_{r=R_0} + R_1 \left.\frac{\partial^2 \phi_0}{\partial r^2}\right)_{r=R_0}, \tag{2.10}$$

$$\left.\frac{\partial \phi_1}{\partial r}\right)_{r=R_0+R_1} \approx \left.\frac{\partial \phi_1}{\partial r}\right)_{r=R_0}. \tag{2.11}$$

Hence KBC to be imposed on $r = R_0(t)$, for the zeroth order, is

$$\frac{\partial \phi_1}{\partial r} = \frac{\partial R_0}{\partial t}, \tag{2.12}$$

and KBC of the first order is, using Eq. (2.6),

$$\frac{\partial \phi_1}{\partial r} = \frac{\partial R_1}{\partial t} + R_1 \frac{M}{R_0^2}. \tag{2.13}$$

In addition, combining Eqs. (2.7) and (2.12) obtains the following expressions for M:

$$M = R_0 \dot{R}_0, \tag{2.14}$$

$$\dot{M} = \dot{R}_0 \dot{R}_0 + \ddot{R}_0 R_0. \tag{2.15}$$

The dynamic boundary condition (DBC) on a free surface at $r = R_0 + R_1$ is

$$\frac{\partial \phi}{\partial t} + \frac{1}{2}|\nabla \phi|^2 + \frac{\kappa}{\mathrm{We}} = \Delta P_0, \tag{2.16}$$

where κ denotes the curvature of the interface and ΔP_0 the pressure adjustment. The Weber number We is given by $\mathrm{We} = \rho^* U^* R^{*2} / \sigma^*$, ρ^* and σ^* being the density and the surface tension of the liquid, respectively. The curvature κ is expressed as, to the first order,

$$\kappa \approx \frac{1}{R_0} - \frac{1}{R_0^2}\left(R_1 + \frac{\partial^2 R_1}{\partial \theta^2}\right). \tag{2.17}$$

Domain perturbation is again applied to DBC to obtain a condition for the unperturbed interface. DBC to be imposed on $r = R_0(t)$ for the first order is

$$R_1\left(\frac{\dot{M}}{R_0} - \frac{M^2}{R_0^3}\right) + \frac{\partial \phi_1}{\partial t} + \frac{M}{R_0}\frac{\partial \phi_1}{\partial r} - \frac{1}{\mathrm{We}}\frac{1}{R_0^2}\left(R_1 + \frac{\partial^2 R_1}{\partial \theta^2}\right) = 0. \tag{2.18}$$

As a solution of the Laplace equation, ϕ_1 is expressed as a superposition of normal modes:

$$\phi_1 = \sum_{m=1}^{\infty} A_m(t) r^m \cos m\theta, \tag{2.19}$$

where only sinusoidal perturbations are considered. Choosing a potential which corresponds to a disturbance decreasing away from the interface in the inward direction (Plesset 1954) eliminates terms having r^{-m} from the solution of the Laplace equation. Consequently, the shape perturbation is given by

$$R_1 = \sum_{m=1}^{\infty} f_m(t) \cos m\theta. \tag{2.20}$$

Substitution of Eqs. (2.19) and (2.20) into Eq. (2.13) yields

$$m A_m R_0^{m-1} = \dot{f}_m + \frac{M}{R_0^2} f_m. \tag{2.21}$$

After substituting Eqs. (2.19) and (2.20), Eq. (2.18) becomes,

$$f_m\left[\frac{\dot{M}}{R_0} - \frac{M^2}{R_0^3} + \frac{(m^2-1)}{\mathrm{We}}\frac{1}{R_0}\right] + R_0^m \dot{A}_m + mMR_0^{m-2}A_m = 0. \tag{2.22}$$

Combining Eqs. (2.21) and (2.22), we finally obtain an equation for the shape perturbation amplitude f_m:

$$\ddot{f}_m + a(t)\dot{f}_m + b(t) f_m = 0, \tag{2.23}$$

where a and b are given as the following, by virtue of Eqs. (2.14) and (2.15):

$$a(t)=2\frac{\dot{R}_0}{R_0}, \tag{2.24}$$

$$b(t)=\frac{(m+1)}{R_0^3}\left[\frac{m(m-1)}{\mathrm{We}}+R_0^2\ddot{R}_0\right]. \tag{2.25}$$

In a special case where R_0 is kept at unity throughout time, the frequency for the mth mode perturbation, ω_m, is given by

$$\omega_m^2=\left[\frac{m(m^2-1)}{\mathrm{We}}\right]^{1/2}, \tag{2.26}$$

which is identical to Chandrasekhar's result (1961). See Appendix B for details.

In short, Eq. (2.23) describes the development of a nonaxisymmetric perturbation on a cylindrical spreading sheet. The coefficients are known if the spreading dynamics are known. We note that Eq. (2.23) is a second order linear ordinary differential equation with variable coefficients. This equation cannot be solved analytically, although stability of the solution can be obtained for limit cases when the coefficients are periodic functions of t.

2.3. Numerical simulation results

We begin to investigate the instability by obtaining the base flow solutions. According to Bowden and Field's model (1964), we expect a nearly immediate generation of a liquid sheet on impact when the Mach number, $\mathrm{Ma}=U^*/c^*$, U^* being the impact velocity and c^* the sound speed in the liquid medium, is very small. However, due to a lack of quantitative empirical data on the behavior of droplets immediately after impact, we resort to simple models to obtain the base flow solutions.

To obtain the base flow solution, i.e., the expansion rate of the liquid sheet or contact area, consider the following limiting case. Suppose that the descending speed of a droplet after impact is invariant from its original speed, which is often observed in the early stages of spreading (Stow and Hadfield 1981, Thoroddsen and Sakakibara 1998). As shown in Figure 2.3 (a), we assume that the bottom of the spherical droplet is displaced to the periphery of the droplet spreading on the surface, resulting in a shape of

truncated-sphere-on-cylinder. Using volume conservation, the radius of the cylinder or contact radius is calculated to be

$$\xi_1 = \left[\frac{3}{2} - \frac{9}{8}s^2 - \frac{1}{2}\left(\frac{81}{16}s^4 - \frac{27}{2}s^2 + 12s - 3\right)^{1/2}\right]^{1/2}, \tag{2.27}$$

where $s = 1 - t$ $(0 < t < 1/3)$. For $t << 1$, $\xi_1 \approx 2t^{1/2}$. It is interesting to note that if the droplet continues to travel after hitting the surface as if it did not exist (See Figure 2.3 (b)), the radius of intersecting area is expressed as $\xi_2 = (2t - t^2)^{1/2}$, which is approximated to be $\xi_2 = (2t)^{1/2}$ for $t << 1$. We suppose that the expanding liquid sheet exhibits the same tendency as ξ's modeled above, then we write

$$R_0 = At^{1/2}, \tag{2.28}$$

where the coefficient A is to be determined empirically for each impact situation. Figure 2.4 shows radius and deceleration profiles depending on the value of A.

In the context of the Rayleigh-Taylor instability, when the expanding liquid decelerates with respect to a lighter atmospheric gas, the liquid tends to be destabilized while the surface tension has a stabilizing effect. It is also possible to approximately predict stability by observing the behavior of the coefficients a and b. Figure 2.5 shows a and b as functions of time based on Eq. (2.28). In general, positive a, as shown in Figure 2.5 (a), corresponds to the positive energy dissipation, thus it has stabilizing effect. On the other hand, b, the restoring term, is negative at small t for all wave numbers shown in Figure 2.5 (b), thus destabilizing the interface. As the wave number increases, b becomes positive during spreading due to the presence of surface tension, thus stabilizing the corresponding perturbation.

However, only numerical simulation can exactly predict the most dangerous wave number and the rate of growth for the shape perturbation because of the time dependent coefficients of Eq. (2.23). Based on the base solutions, we numerically solve Eq. (2.23) under given initial conditions such as $f_m = 1$ and $\dot{f}_m = 0$, and $f_m = 0$ and $\dot{f}_m = 1$. The modified Euler method has been employed to solve the initial value problem (Nakamura 1991).

Factors which determine the magnitude of deceleration of a liquid interface, i.e., the driving mechanism of the Rayleigh-Taylor instability, include the initiation time of perturbation as well as the coefficient A. Mathematical singularity occurs as $t \to 0$ when

both the velocity and the deceleration of the sheet reach infinity. The sheet emerges from a finite initial radius which corresponds to a finite nonzero initiation time. Since there are no conclusive experimental data on exactly when the liquid sheet emerges, we examine the sensitivity of the perturbation analysis to the perturbation onset time t_i. On the other hand, effects of impact inertia and surface tension are manifested through the Weber number in our analysis. The presence of surface tension that stabilizes the interface leads to the mode of maximum instability. In the following we present the numerical simulation results including the roles of such parameters as described above.

Figure 2.6 shows the temporal evolution of shape perturbations for different wave numbers. For a computation time range, we use the limit to which Eq. (2.27) holds, i.e., t=1/3. Perturbations of different wave numbers compete with one another and the mode number of maximum instability varies with time, unlike time-independent coefficient systems. In addition, neither the growth rate of the perturbation nor the cutoff wave number is easily defined. As predicted in Figure 2.5, the perturbations of high wave numbers are stabilized as t increases although the instants when the amplitudes alter their slopes do not exactly coincide with those at which the b's change sign.

Figure 2.7 (a) shows that there exists a wave number which maximizes the amplitude perturbation at every moment during spreading. Furthermore, the number tends to decrease during spreading (Figure 2.7 (b)). More studies are required to understand how fingers merge during spreading and which wave number manifests itself in the competition of many modes during spreading. Such questions can be answered by considering nonlinear effects of finite amplitude perturbations, which are beyond the scope of the present work. However, it is clear that high wave numbers excited in earlier stages are overwhelmed by lower wave numbers in the course of spreading as deceleration gradually comes to a stop. It is also noted that disturbances of very high wave numbers are rapidly stabilized by surface tension. Figure 2.8 shows the growth of azimuthal disturbances at the modes of maximum instability based on the simulation results. A droplet with a higher Weber number (Figure 2.8 (b)) develops more unstable spreading front than one with a lower Weber number (Figure 2.8 (a)).

Effects of the coefficient A, or the expansion rate of the liquid sheet, on instability are shown in Figure 2.9. We note that when the sheet radius is given by Eq. (2.28), a high expansion rate due to large A results in a high magnitude of deceleration, which eventually promotes the instability of higher wave numbers. Figure 2.10 illustrates the effect of perturbation onset time on instability. Perturbations initiated earlier exhibit larger deceleration thus promoting instability of higher wave number. However, it is noteworthy that the analysis results are rather insensitive to t_i. Figure 2.11 presents the

role of the Weber number on the instability. As Weber number increases, that is, when the effect of surface tension is weakened and that of inertia strengthened, the higher wave numbers are more excited. This is consistent with Thoroddsen and Sakakibara's (1998) observation that higher impact speed results in greater finger numbers. Appendix C shows a relevant experimental evidence.

2.4. Conclusions

We developed a linear perturbation theory of interface instabilities of a radially-expanding, liquid sheet in cylindrical geometries. The theory was applied to an expanding sheet under a spreading droplet to elucidate the origin of splashing. The base flow solutions were estimated by using mass conservation. It was shown that significant deceleration occurs in the early stages of spreading, which triggers the Rayleigh-Taylor instability. The model supposes that the main factor inducing deceleration is not viscosity but the continuity of flow around the impact region. The theory was able to predict the most rapidly growing mode of azimuthal disturbance and its growth rate at each instant during spreading. It was found that the mode number of maximum instability changes because of time-dependent coefficients in the amplitude equation. We examined effects of several parameters on the analysis results including the transient profile of an interface radius, i.e. the coefficient A, the perturbation onset time, t_i, and Weber number.

It is noted that the parameters examined above, A, t_i, and We, are interrelated with each other in reality: the impact inertia and surface energy not only affect the Weber number but also determine the collapsing dynamics of the droplet and sheet expansion characteristics: A and t_i. In addition, it is known that substrate roughness plays a significant role in splashing (Stow and Hadfield 1981). The roughness may affect the values of A and t_i and change the mode of the maximum instability as well as destabilize the perturbation of a given wave number. On the other hand, the effects of thermal conditions of the target surface are to be considered especially when a droplet hits a surface as hot as its boiling temperature (Chandra and Avedisian 1991) or when a molten droplet impinges on a subcooled target (Pasandideh-Fard 1998). Understanding these topics calls for more studies in the future.

In conclusion, we find that the rapidly expanding liquid sheet released upon droplet collision with a solid target is subjected to Rayleigh-Taylor instability. Numerical computations of the transient evolution of shape perturbations are able to determine the most rapidly growing wave number and the growth rate of perturbation

amplitudes. Our analysis reveals that larger impact inertia associated with higher We, and thus presumably higher A, promotes interface instability and prefers higher wave number for maximum instability. However, further analysis is required to accurately determine the correlation between the sheet expansion profile and impact conditions. We relate this instability with the fundamental mechanism of splashing from the viewpoint that the inherent feature of splashing is an unstable expansion of the spreading front of droplets.

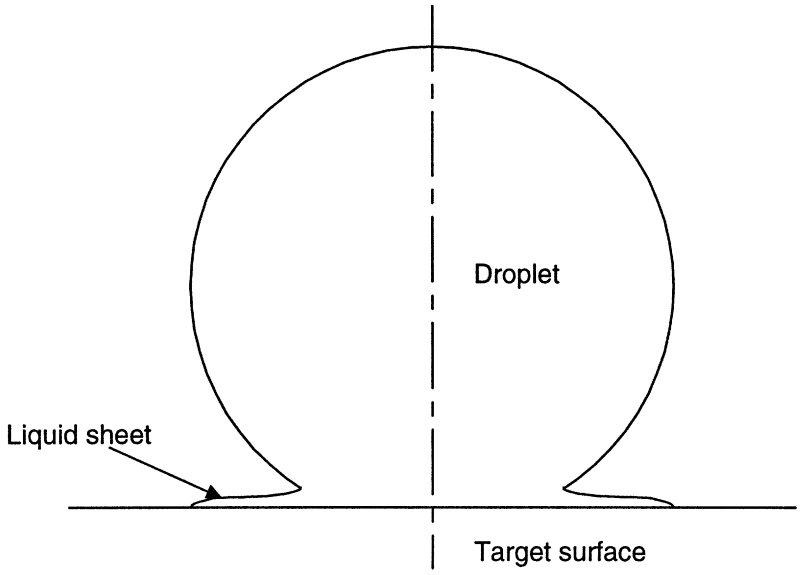

FIGURE 2.1. Release of a liquid sheet upon droplet collision with a solid target.

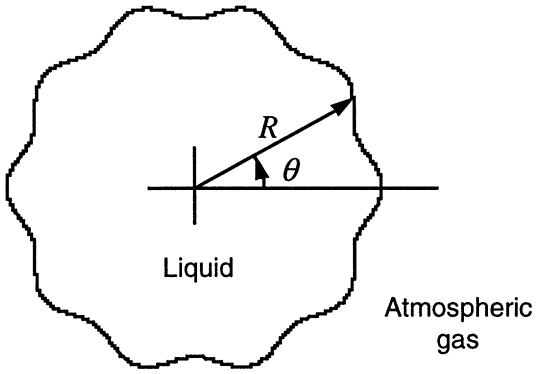

FIGURE 2.2. Disturbed liquid sheet which expands radially.

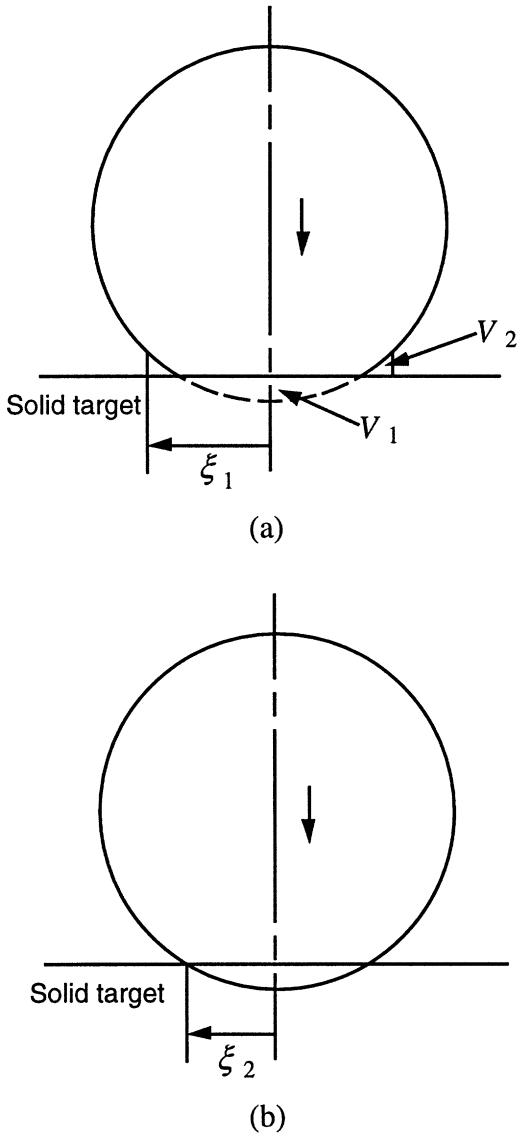

FIGURE 2.3. Limiting cases of droplet spreading. The original droplet radius and velocity are both unity after nondimensionalization. (a) Volume V_1 is displaced to V_2 while the droplet descends with the speed of unity. The cylinder radius ξ_1 is expressed as Eq. (23). (b) ξ_2 is the intersection radius of the target surface and the droplet traveling with no deformation.

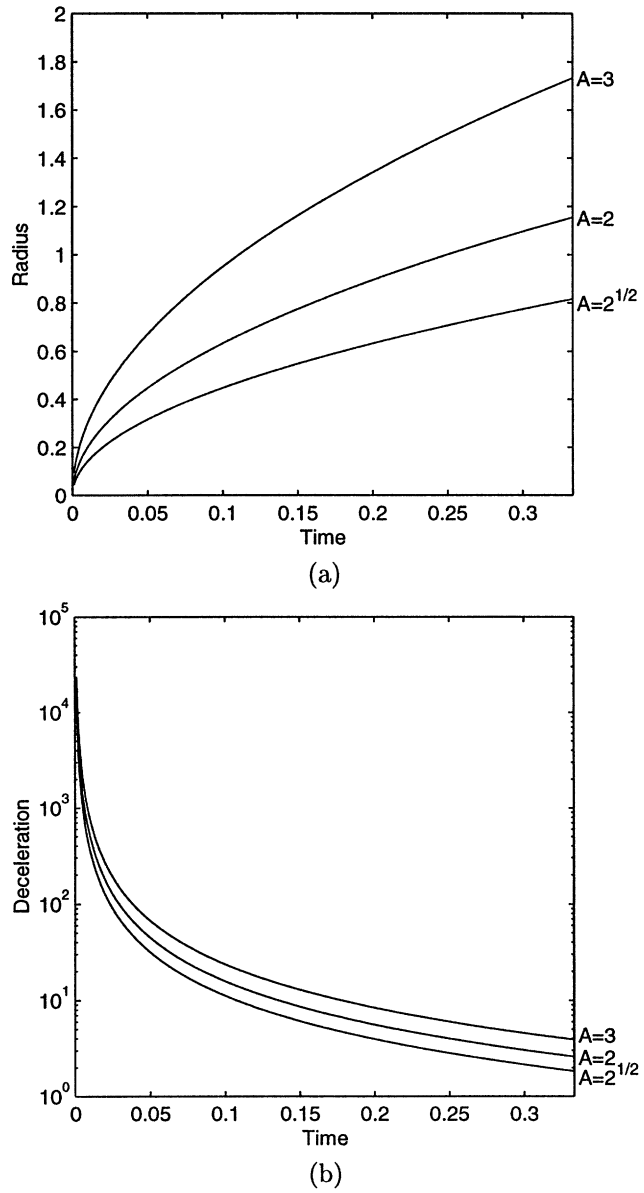

FIGURE 2.4. (a) Transient radius profiles of an expanding liquid sheet expressed as $R_0 = At^{1/2}$. (b) Corresponding deceleration. Note that the significant deceleration is experienced by the interface immediately after impact, which drives the Rayleigh-Taylor instability.

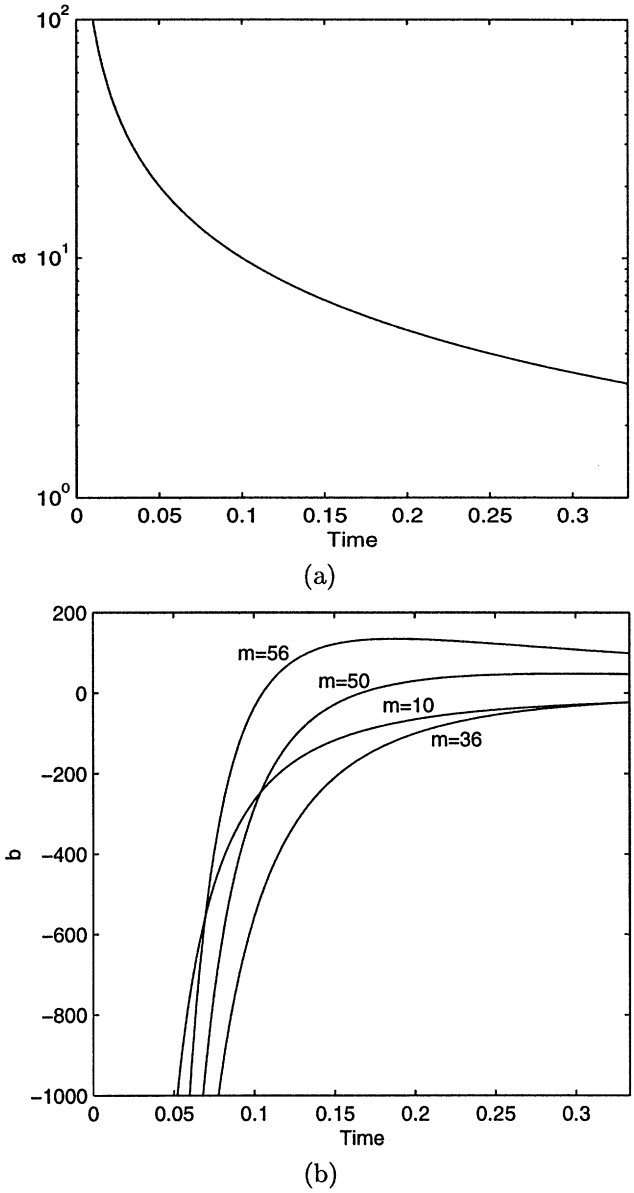

FIGURE 2.5. The coefficients of Eq. (2.23) when $R_0 = 2t^{1/2}$ and We = 500. (a) The coefficient a is given by $a = 1/t$. (b) The coefficient b vs. time for various wave numbers.

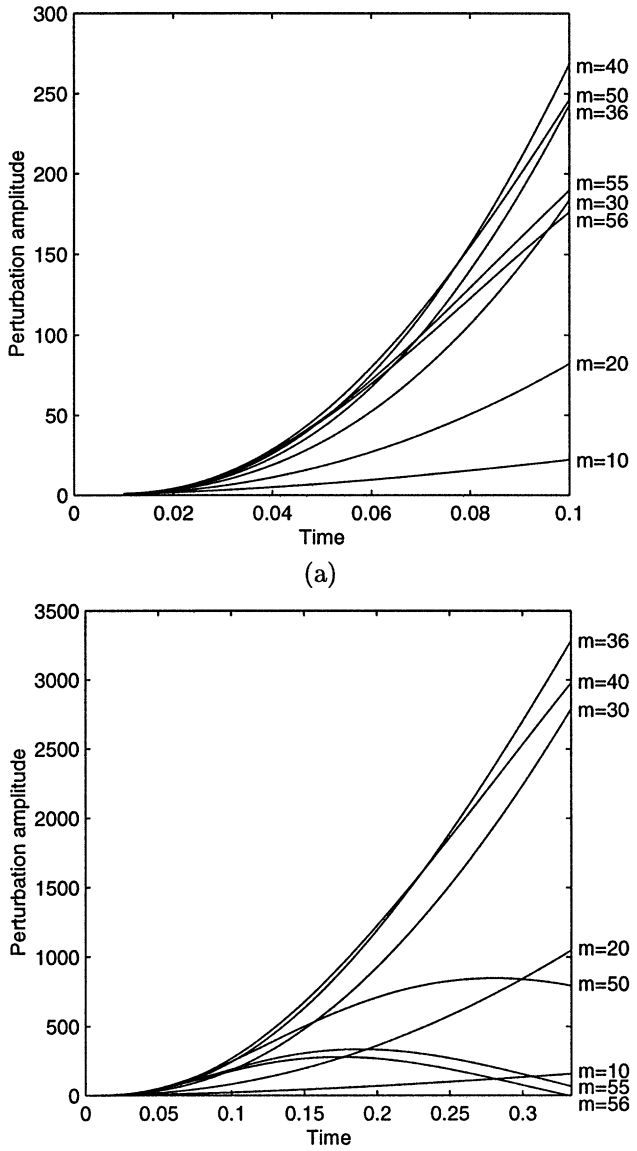

FIGURE 2.6. (a) Temporal evolution of the shape amplitudes of various wave numbers until $t = 0.1$. (b) Temporal evolution of the shape amplitudes until $t = 1/3$. Initial conditions at $t = t_i$ are $f_m = 1$ and $\dot{f}_m = 0$. The computation was performed for $R_0 = 2t^{1/2}$, $t_i = 0.01$, and We $= 500$. Perturbations of $m = 40$ and 50 are exceeded by that of $m = 36$ during spreading. Perturbations of $m = 50, 55$, and 56 decay after initially growing period. The perturbation amplitude of $m = 56$ even decays to the value less than the initially assigned one before t reaches $1/3$. We define a wave number, which is less than the so-found wave number by one, as a pseudo-cutoff wave number - in this case, it is 55.

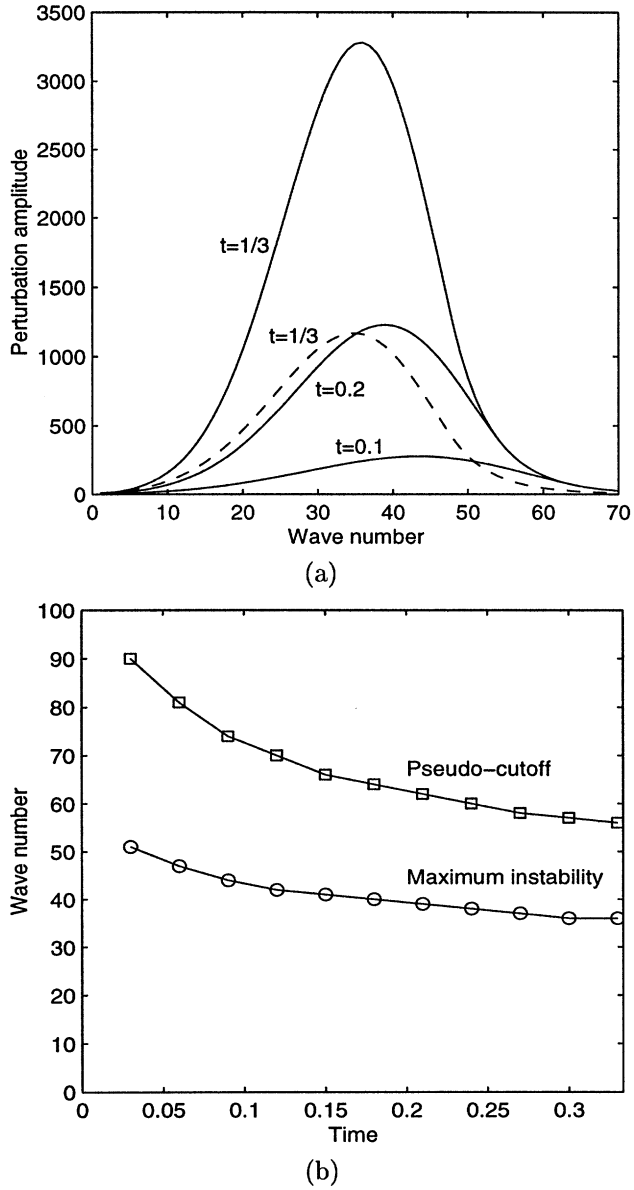

FIGURE 2.7. (a) Perturbation amplitude vs. wave numbers for different time. Initial conditions for solid lines are $f_m = 1$ and $\dot{f}_m = 0$. Initial conditions for a dotted line are $f_m = 0$ and $\dot{f}_m = 100$. The computation was performed for $R_0 = 2t^{1/2}$, $t_i = 0.01$, and We $= 500$. (b) Changes of a mode number of maximum instability and a pseudo-cutoff wave number with time. Computation conditions are those of the solid lines in (a).

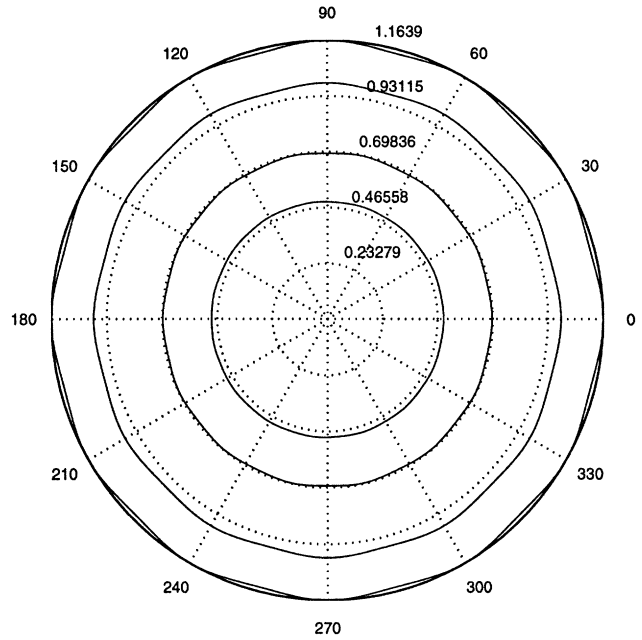

(a)

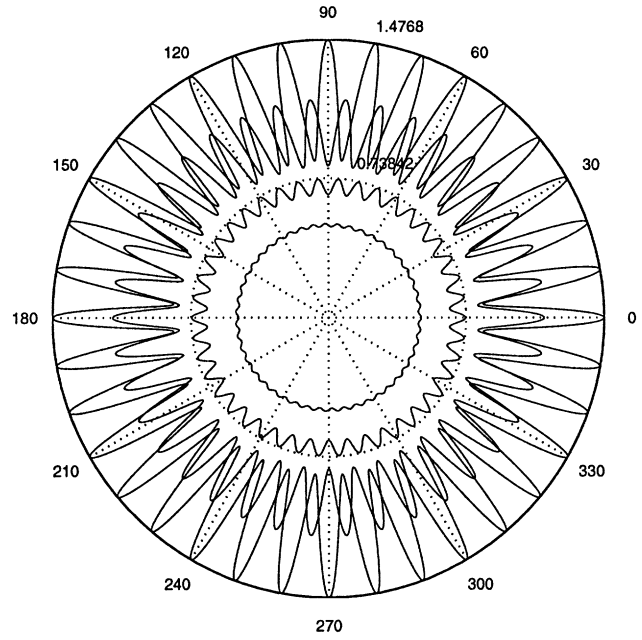

(b)

FIGURE 2.8. Growth of azimuthal disturbances during spreading at the modes of maximum instability. Initial conditions are $f_m = 1 \times 10^{-4}$ and $\dot{f}_m = 0$. The computation was performed for $R_0 = 2t^{1/2}$ and $t_i = 0.01$. (a) Shape evolutions when We = 50. From the innermost corrugated circle, $t = 0.06$ ($m = 15$), 0.12 ($m = 14$), 0.24 ($m = 12$), and 1/3 ($m = 12$). (b) Shape evolutions when We = 500. From the innermost corrugated circle, $t = 0.06$ ($m = 47$), 0.12 ($m = 42$), 0.24 ($m = 38$), and 1/3 ($m = 36$).

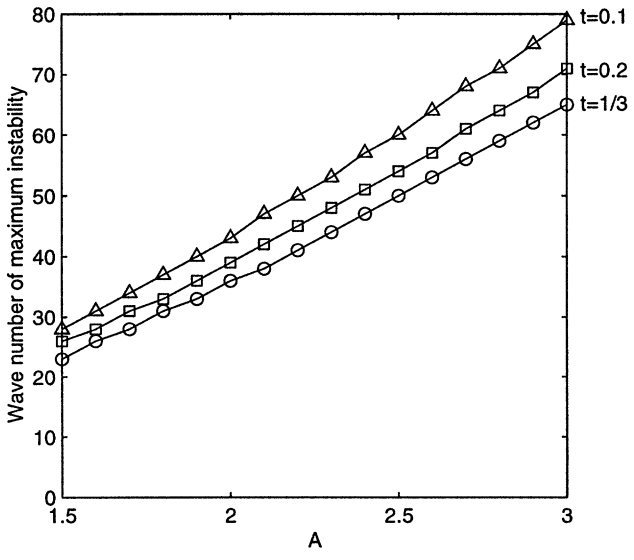

(a)

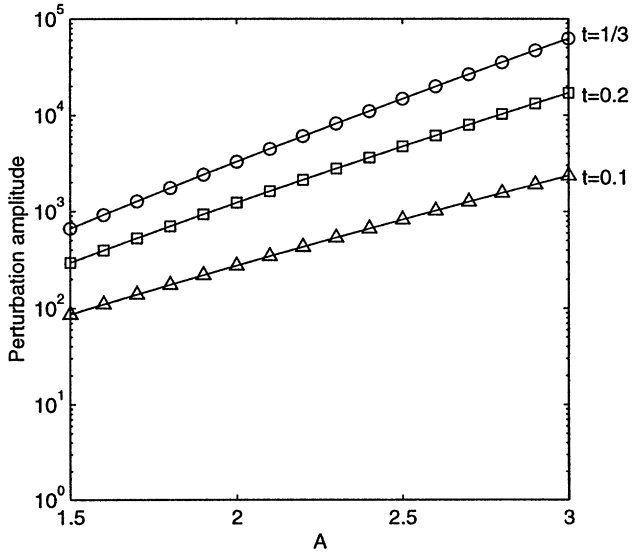

(b)

FIGURE 2.9. Effect of the coefficient A on instability. (a) Wave number of maximum instability vs. A. (b) Perturbation amplitude of those numbers vs. A.

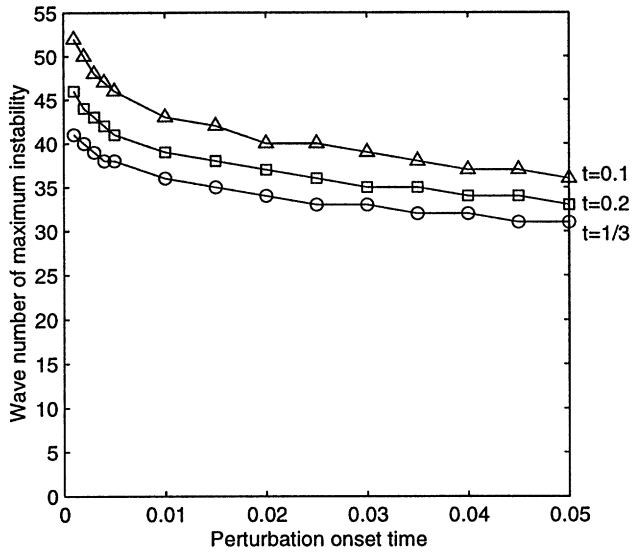

(a)

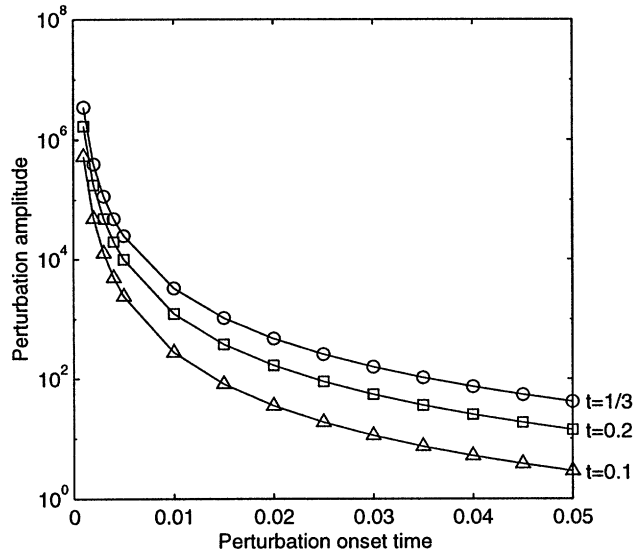

(b)

FIGURE 2.10. Effect of the perturbation onset time t_i on instability. (a) Wave number of maximum instability vs. t_i. (b) Perturbation amplitude of those numbers vs. t_i.

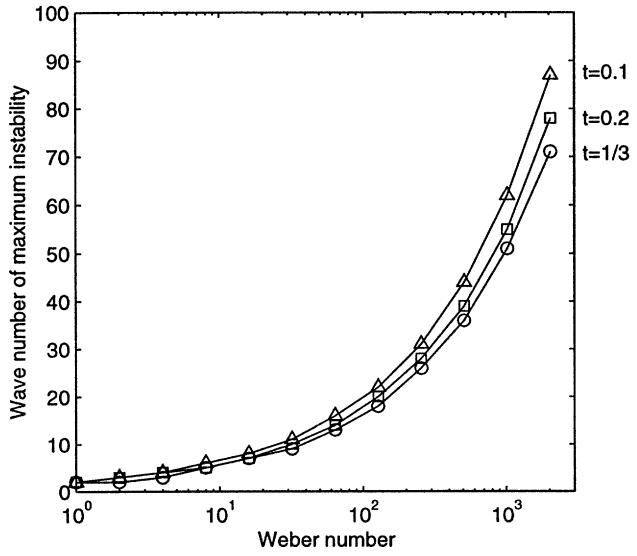

(a)

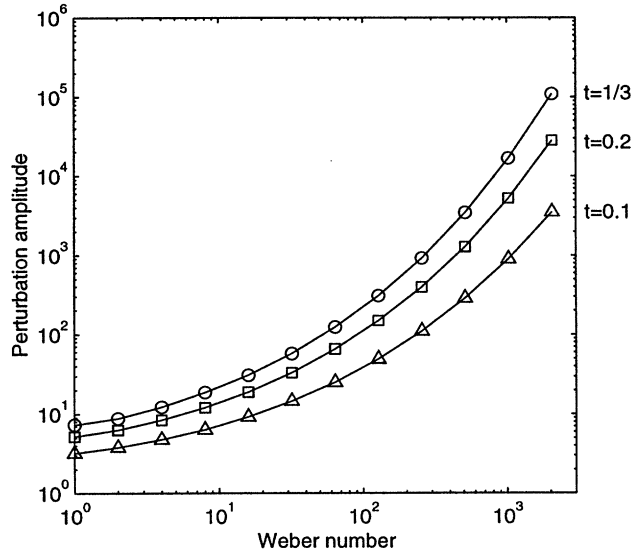

(b)

FIGURE 2.11. Effect of Weber number on instability. (a) Wave number of maximum instability vs. We. (b) Perturbation amplitude of those numbers vs. We.

CHAPTER 3

THE OSCILLATION OF LIQUID DROPLETS UPON COLLISION WITH SOLID SURFACES

3.1. Introduction

This chapter investigates the oscillations of liquid droplets upon collision with solid surfaces which depend on various dynamic and wetting conditions. The post-impact oscillations of a liquid droplet consist of the initial spreading of the droplet until it reaches its maximum base diameter and subsequent oscillatory motions of recoiling and re-spreading. Dynamics of liquid droplets colliding with solid surfaces have been extensively studied for more than a century (Worthington 1877a,b). However, the majority of this effort has been focused on the initial spreading process, i.e. from the moment of impact to the moment when the droplet reaches its maximum base diameter (Engel 1955; Harlow and Shannon 1967; Stow and Hadfield 1981; Tsurutani et al. 1990; Trapaga and Szekely 1991; Shi and Dear 1992). As a result, it appears to be only recent that the post-impact oscillations gained the full interests of the scientific communities.

Fukai et al. (1995) conducted a theoretical study on the spreading and recoiling of a liquid droplet upon colliding with a solid surface. In the study, the numerical simulation results were compared with experimental data that used water droplets and Pyrex glasses of different surface roughness and a wax coating as the target materials. To account for the effects of wetting, different values for the advancing and receding contact angles, measured while allowing droplets to slide down an inclined test surface, were adopted per target material. Their model is based on solving the full Navier-Stokes equation by utilizing deforming finite elements and allowing the contact line to slip. Their prediction was generally in good agreement with experimental measurements. Pasandideh-Fard et al. (1996) performed a similar study by numerically solving the full Navier-Stokes equation using a modified SOLA-VOF method and a no-slip boundary condition. In the experiments, droplets of water with different surfactant concentrations were deposited on polished, stainless steel surfaces. Dynamic contact angles were measured from photographs and the values were used as a boundary condition for the numerical model. Their model accurately predicted experimental measurements taken during the initial spreading stages. However, a discrepancy was found during the recoiling stages. Zhang and Basaran (1997) performed an experimental study using

distilled water and aqueous surfactant solutions as the droplet material and glass as the target surface. They measured the long-time behavior, i.e., oscillation, of a liquid droplet using high speed video. They found that the decrease of surface tension due to the presence of a surfactant enhanced the spreading while Marangoni stresses induced by non-uniform surfactant distribution inhibited the spreading.

Studies of the oscillation dynamics of sessile and pendant drops began only recently. The reader is referred to an extensive review on the subject by Wilkes and Basaran (1997). Since the studies concern the motion of supported droplets, i.e., drops placed on solid supports *a priori.*, the effect of impingement with the solids on the droplet dynamics is beyond the scope of the studies. Schiaffino and Sonin (1997) discussed the oscillations of a droplet's centerline elevation after its footprint is arrested by freezing on a subcooled target of its own kind. They found that the oscillation damping time of deposited water droplets is in good agreement with the damping time of a negligibly viscous, liquid drop which oscillates freely.

Our theoretical study is motivated by an approach, originated by Kendall and Rohsenow (1978) and Bechtel et al. (1981), to the dynamics of the droplet impact. The approach is based on the variational principle rather than on the Navier-Stokes equation which requires significant computational efforts. Its advantage is that by assuming the geometry of the deforming droplet, a very simple differential equation is obtained to describe the droplet dynamics. From the experimental aspect, the current study aims to investigate the spreading and subsequent oscillations of various liquid droplets upon collision with different solid surfaces. Although similar experimental studies have been performed by previously mentioned authors (Fukai et al.; Pasandideh-Fard et al.; and Zhang and Basaran), this study not only examines a broad spectrum of dynamic impact conditions such as Weber number and Reynolds number, but also investigates the wetting effects caused by various combinations of liquid droplets and solid targets. In this chapter, we compare the modeling results and the experimental measurements to show the capability of our model to predict the complicated phenomena of the droplet spreading.

3.2. Modeling

We model the oscillations of a droplet by adopting the variational principle instead of solving the Navier-Stokes equation with moving boundaries. We assume two different droplet shapes in performing the variational method, i.e., a cylinder and a truncated sphere. We derive the cylinder model in a similar manner to Kendall and Rosehnow's

model (1978). Our model extends theirs to include the wetting properties of the liquid droplet with a solid surface and the frictional dissipation. In addition, the initial conditions are determined to satisfy the energy conservation exactly. A variational method using a truncated sphere was derived by Bechtel et al. (1981), and we briefly introduce their results as well with further modifications.

3.2.1 *Formulation of the problem using a cylinder model*

The variational principle can be written as (Crandall et al. 1968):

$$\int_{t_1}^{t_2}\left(\delta T^* - \delta V^* + \delta W_f^*\right)\mathrm{d}t^* = 0, \tag{3.1}$$

where T^* denotes the kinetic coenergy, V^* the potential energy, and t^* the time. The frictional work δW_f^* is expressed as

$$\delta W_f^* = -F^*\delta y^*, \tag{3.2}$$

where F^* denotes the frictional force and y^* the displacement of the frictional motion. In a case where the frictional force is due to the wall shear stress, we write Eq. (3.1) as

$$\int_{t_1}^{t_2}\left[\delta\left(T^* - V^*\right) - \int_{A_b^*}\tau^*\delta\Delta_r^*\mathrm{d}A^*\right]\mathrm{d}t^* = 0, \tag{3.3}$$

where τ^* is the shear stress at the base of the droplet, Δ_r^* the radial displacement, and A_b^* the base area. Each term in the integrand can be evaluated when the shape of the deforming droplet and the velocity profile are known. The initial velocity and the diameter of the original droplet before collision are U^* and D^*, respectively. The droplet has the density ρ^*, the surface tension σ^*, and the viscosity μ^*. We choose D^*, $\left(\rho^* D^*/\sigma^*\right)$, and U^* as the characteristic length, time and velocity scales, respectively. The following quantities are nondimensionalized based on those scales unless noted otherwise, and their forms are summarized in Appendix D.

We model the oscillating droplet on a solid surface as a cylinder whose base diameter and height are D_b and h, respectively, as shown in Figure 3.1. The volume of the cylinder is the same as that of the droplet, thus

$$D_b^2 h = \frac{2}{3} \tag{3.4}$$

is satisfied for any t. If either D_b or h is specified in time, the other is known straightforwardly by Eq. (3.4). Therefore, it is enough to simulate the temporal evolution of either D_b or h to fully describe the dynamics of the oscillating cylinder. We derive the equation for h in the following.

Assuming axisymmetric motion, the nondimensional kinetic coenergy is written as

$$T = \int_V \left(v_z^2 + v_r^2\right) \mathrm{d}Vol, \tag{3.5}$$

where v_z and v_r denote the axial and radial velocity of the flow inside the cylinder, respectively, and Vol is the volume. For the energy and volume scales, we choose $\pi\rho^* D^{*3} U^{*2}/12$ and $\pi D^{*3}/6$, which correspond to the original kinetic coenergy and the volume of the colliding droplet, respectively. We relate the axial velocity v_z with h as

$$v_z = \frac{1}{\mathrm{We}^{1/2}} \frac{z}{h} \frac{\mathrm{d}h}{\mathrm{d}t}, \tag{3.6}$$

where We is the Weber number defined as $\mathrm{We} = \rho^* U^{*2} D^* / \sigma^*$. The radial velocity v_r is given by continuity as

$$v_r = -\frac{1}{2} \frac{1}{\mathrm{We}^{1/2}} \frac{r}{h} \frac{\mathrm{d}h}{\mathrm{d}t}, \tag{3.7}$$

where r is the nondimensional radius. The flow field given by Eq. (3.6) and (3.7) is that of the potential flow which satisfies the Laplace equation. Substituting Eqs. (3.6) and (3.7) into Eq. (3.5) and performing integration over the volume of the cylinder, we obtain

$$T = \frac{1}{3} \frac{1}{\mathrm{We}} \left(\frac{\mathrm{d}h}{\mathrm{d}t}\right)^2 \left(1 + \frac{1}{16h^3}\right). \tag{3.8}$$

In evaluating the potential energy we do not include gravity since we are mainly interested in the oscillation due to interfacial phenomenon. Hence the potential energy V is written as

$$V = \frac{3}{\mathrm{We}} D_b^2 \left[\frac{4h}{D_b} + (1 - \cos\theta) \right], \tag{3.9}$$

where • is the equilibrium contact angle between the liquid droplet and the solid surface. By using Eq. (3.4), we express the potential energy as

$$V = \frac{2}{\mathrm{We}} \left[2(6h)^{1/2} + \frac{(1 - \cos\theta)}{h} \right]. \tag{3.10}$$

The dissipative work is estimated in the same manner as Bechtel et al. (1981). Since the potential flow field we obtained does not afford the viscous effects, we estimate the external viscous stress, τ^*, based on that of the oscillating stagnation flow with the period t^*. Defining the characteristic hydrodynamic boundary layer thickness δ_H^* as

$$\delta_H^* = D^* \left(\frac{1}{\pi^2} \frac{\mathrm{We}}{\mathrm{Re}^2} \right)^{1/4}, \tag{3.11}$$

we write

$$\tau = F_d \frac{v_r}{\delta_H}, \tag{3.12}$$

where F_d is the dissipation factor. We choose $\mu^* U^* / D^*$ as the characteristic stress scale. Substitution of Eq. (3.7) into Eq. (3.12) yields

$$\tau = -\frac{F_d}{2\delta_H \mathrm{We}^{1/2}} \frac{r}{h} \frac{\mathrm{d}h}{\mathrm{d}t}. \tag{3.13}$$

The radial displacement Δ_r is written, in the present nondimensionalization, as:

$$\Delta_r = \frac{U^* \tau^*}{D^*} \int v_r \mathrm{d}t. \tag{3.14}$$

Substituting Eq.(3.7) into Eq. (3.14) we obtain

$$\Delta_r = -\frac{1}{2} r \ln h , \tag{3.15}$$

where we arbitrarily set the integration constant to zero since $\delta\Delta_r$ is of our interest.

Performing the variation of the kinetic coenergy with respect to h and using integration by parts, we get

$$\int_{t_1}^{t_2} \delta T \mathrm{d}t = -\frac{1}{3\mathrm{We}} \int_{t_1}^{t_2} \left[2\frac{\mathrm{d}^2 h}{\mathrm{d}t^2}\left(1+\frac{1}{16h^3}\right) - \frac{3}{16}\left(\frac{\mathrm{d}h}{\mathrm{d}t}\right)^2 \frac{1}{h^4} \right] \delta h \mathrm{d}t . \tag{3.16}$$

By a similar procedure, we obtain

$$\delta V = \frac{2}{\mathrm{We}} \left[6^{1/2} h^{-1/2} - (1-\cos\theta) h^{-2} \right] \delta h , \tag{3.17}$$

and

$$\delta W_f = \frac{1}{24} \frac{F_d}{\delta_H \mathrm{ReWe}^{1/2}} \frac{1}{h^4} \left(\frac{\mathrm{d}h}{\mathrm{d}t} \right) \delta h . \tag{3.18}$$

On substituting Eqs. (3.16), (3.17), and (3.18) into Eq. (3.3), we require that the coefficient of δh should be zero for the variational formula to be satisfied. After arrangement, we obtain an equation to describe the temporal evolution of h:

$$\ddot{h} - B(h)\dot{h}^2 + C(h)\dot{h} + D(h) = 0 , \tag{3.19}$$

where the dot denotes the first derivative with respect to the time and the double dots the second derivative. The coefficients are given by

$$B(h) = \frac{3}{32} h^{-1} \left(h^3 + \frac{1}{16} \right)^{-1} , \tag{3.20}$$

$$C(h)=\frac{2}{3}B(h)\frac{\mathrm{We}^{1/2}}{\delta_H \mathrm{Re}}, \tag{3.21}$$

and

$$D(h)=21B(h)\left[6^{1/2}h^{7/2}-(1-\cos\theta)h^2\right]. \tag{3.22}$$

The initial conditions, i.e., h and $\dot{h}$ at t = 0, should be specified to solve Eq. (3.19). Since the original droplet and a cylinder have a substantial difference in shape, we seek initial conditions which ensure that the initial kinetic coenergy and potential energy of the cylinder are the same as those of the original droplet. In addition, the volume must be conserved as stated in Eq. (3.4). The equality of initial potential energies of the original droplet and a cylinder yields the following relation:

$$h(0)=\frac{1}{D_b(0)}-\frac{(1-\cos\theta)}{4}D_b(0). \tag{3.23}$$

Further arrangement of Eq. (3.23) is made by using Eq. (3.4):

$$\frac{(1-\cos\theta)}{8}D_b^3(0)-\frac{1}{2}D_b(0)+\frac{1}{3}=0. \tag{3.24}$$

Therefore, Eqs. (3.24) and (3.4) determine the initial diameter and height of the cylinder. The initial $\dot{h}$ is given by the equality of the kinetic coenergies:

$$\dot{h}(0)=-\mathrm{We}^{1/2}\left\{\frac{1}{3}+\frac{1}{32}\left[\frac{D_b(0)}{h(0)}\right]^2\right\}^{-1/2}. \tag{3.25}$$

We note that the initial diameter and height of the cylinder depends solely on the contact angle θ, and Figure 3.2 shows $D_b(0)$ and h versus θ.

Summarizing our problem formulation, the second order nonlinear differential equation, Eq. (3.19), completely describes the dynamics of a liquid cylinder oscillating on a solid surface. The initial value problem can be solved numerically with the initial conditions specified by Eqs. (3.23), (3.24), and (3.25).

3.2.2. *Formulation of the problem using a truncated sphere model*

We briefly present Bechtel et al.'s truncated sphere model in this section with the estimation of the frictional term modified. The geometry of a truncated sphere is shown in Figure 3.3. They assumed the same velocity profiles as we did in the cylinder model above, and the equation for the temporal evolution of h is given by

$$2A(h)\ddot{h} - C(h)\dot{h}^2 + D(h)\dot{h} + E(h) = 0, \tag{3.26}$$

where the coefficients are given by

$$A(h) = \left[\frac{M'(h)}{M(h)}\right]^2 \left(\frac{13}{180}h^5 + \frac{11}{144}h^2 + \frac{1}{72}h^{-1}\right), \tag{3.27}$$

$$M(h) = \frac{1}{6}\left(2h + h^4\right), \tag{3.28}$$

$$\begin{aligned} C(h) = &\left(\frac{13h^4}{36} + \frac{11h}{72} + \frac{h^{-2}}{72}\right)\left(\frac{1}{3} + \frac{2h^3}{3}\right)\left(\frac{h}{3} + \frac{h^4}{6}\right)^{-2} \\ &+ \left(\frac{13h^5}{90} + \frac{11h^2}{72} + \frac{h^{-1}}{36}\right)\left(\frac{1}{3} + \frac{2h^3}{3}\right) \\ &\cdot \left[2h^2\left(\frac{h}{3} + \frac{h^4}{6}\right) - \left(\frac{1}{3} + \frac{2h^3}{3}\right)^2\right] \cdot \left(\frac{h}{3} + \frac{h^4}{6}\right)^{-3} \end{aligned} \tag{3.29}$$

$$D(h) = VIS\left(h^4 - 2h + h^{-2}\right)\left(\frac{1}{3} + \frac{2}{3}h^3\right)^2 \left(\frac{h}{3} + \frac{h^4}{6}\right)^{-2}, \tag{3.30}$$

and

$$E(h) = 2\left[4h - h^{-2} - ST\left(2T + h^{-2}\right)\right]. \tag{3.31}$$

The parameters ST and VIS are given, in the present nondimensionalization, by

$$ST = -\cos\theta \tag{3.32}$$

and

$$VIS = \frac{C}{12}\frac{\mathrm{We}^{1/2}}{\mathrm{Re}}, \tag{3.33}$$

where C is related to the boundary layer thickness of an oscillating flow with the period t^* and Re denotes the Reynolds number defined as $\mathrm{Re} = \rho^* U^* D^* / \mu^*$; μ^* being the viscosity. We modify Bechtel et al.'s model to include the dissipation factor, F_d, in the estimation. Thus, C is given by

$$C = \frac{F_d}{\delta_H}, \tag{3.34}$$

where δ_H is given by Eq. (3.11). The base diameter is related to h by

$$D_b = 2\left[\frac{1}{3}\left(h^{-1} - h^2\right)\right]^{1/2}. \tag{3.35}$$

Since the initial droplet shape assumed by this model accurately represents the real spherical shape, the initial conditions are obtained straightforwardly. The initial height is set equal to the original diameter of the droplet and the initial velocity is set equal to the velocity of the droplet prior to collision. After nondimensionalization, we write

$$h(0) = 1, \tag{3.36}$$

and

$$\dot{h}(0) = -\mathrm{We}^{1/2}. \tag{3.37}$$

However, we note that while the exact value of the initial kinetic coenergy is $\pi\rho^* D^{*3} U^{*2}/12$, its value given by this model is $13\pi\rho^* D^{*3} U^{*2}/120$ due to the assumed velocity profile.

3.3. Description of the experimental apparatus

The experimental apparatus is illustrated in Figure 3.4. It consists of a pipette which gently ejects a liquid droplet, a flat target on which the droplet falls, a high-speed video system, and a stroboscope which is synchronized with the video system. As the experimental liquids, deionized water, ink, and silicone oil (Dow Corning 704 diffusion pump oil) are used. Table 3.1 shows the physical properties of the liquids. To examine various collision conditions, the velocity prior to impact is varied by changing the distance between the pipette and the target. In addition, two different sizes of pipettes are used to vary the original droplet diameter. Acrylic and silicone oxide (SiO_2) are used as the target surfaces. The equilibrium contact angles between the liquids and the surfaces are measured to evaluate the wetting characteristics The measurement procedure and the values are presented in Appendix E.

A high speed video system (Kodak Ektapro EM, Model 1012) records the spreading and subsequent oscillation of a droplet on a solid surface at a rate of 1000 frames per second. An image stored in the system consists of 192 X 239 pixels. The illumination is provided by a stroboscope, which is synchronized with the camera; thus, very sharp images are captured. The images stored in the digital memory are downloaded onto a video tape using a S-VHS video tape recorder, and analyzed by an image analysis software which is capable of measuring the dimensions of objects by the number of pixels. An object of a known size (8 mm in diameter) is recorded by the same video setup and used for calibration. In addition, to obtain the highly accurate conditions of the droplet impact, the weight of the droplet is measured during each experiment. The diameter deduced by the weight-measurement method is compared with that obtained by the image calibration. The values are in very close agreement in all cases, with less than 2% discrepancy. Using the image analysis software, we measure the base diameter of the droplet at each frame to determine the temporal evolution of droplet oscillations.

3.4. Experimental and modeling results

In this section, we present experimental observations on the oscillations of different liquid droplets on different target surfaces. In addition, we compare our measurement results with the predictions of the models discussed above. Figure 3.5 shows the dynamics of a water droplet colliding with an acrylic surface. Two very different kinds of dynamic impact behavior are shown in the figure. The oscillating droplet of Figure 3.5 (b) exhibits a much smaller base diameter and thus, higher centerline elevation than that

of (a). The droplet motion after the first oscillation period, i.e., after the first recoiling is completed, is much more vigorous in (b) than (a), as well. It is well known that high impact inertia associated with high Weber number and Reynolds number results in a greater spread factor β. The spread factor is defined as the ratio of the maximum base diameter during spreading to the original droplet diameter: $\beta = D^*_{b,max}/D^*$. A high Weber number also induces an unstable spreading front as observed by other researchers (Allen 1975, Thoroddsen and Sakakibara 1998). In addition, our figures show that high impact inertia, i.e., high We and Re, results in vigorous post-impact oscillations relative to those generated by low inertia impact.

The temporal evolution of the base diameter of the oscillating droplet was measured and the results are shown in Figure 3.6. The vigorous oscillations of the droplet with high impact inertia are clearly observed as well as the increased spread factor in the initial stages of the spreading. Next, we compare the predictions of the models with the experimental data, in Figure 3.7. We present the results of two different models, the cylinder model and the truncated sphere model. Dissipation factors are empirically determined to best fit the experimental data in general. In the low impact inertia case as shown in Figure 3.7 (a), both the cylinder model and the truncated sphere model show qualitatively good agreement with the experimental measurements. Figure 3.7 (b) shows that the cylinder model closely predicts the experimental measurements. However, the truncated sphere model deviates significantly from the experimental data. Figure 3.7 (c), the high impact inertia case, also shows that the cylinder model predicts the experimental results well.

In general, we observe that the cylinder model better predicts the experiments than the truncated sphere model. This is explained by investigating the images in Figure 3.5, which reveals that the recoiling droplet resembles a cylinder more closely than a truncated sphere. Nevertheless, we note that the truncated sphere model succeeds in predicting the initial spreading stage before the droplet reaches the maximum base diameter in all the cases. This is because the truncated sphere represents the shape of the collapsing droplet in the initial stages with sufficient accuracy.

Next, we examine the effect of the target solids on the droplet dynamics. Figures 3.8 (a) and (b) compare the base diameters of water and ink droplets, respectively, on different target surfaces, acrylic and silicon oxide. We note that water and ink commonly wet the silicon oxide surface better than the acrylic surface. Under similar impact conditions, the base diameters in the initial spreading stage are essentially alike. However, in the recoiling stage, the droplet deposited onto the acrylic (poor wetting surface) retracts its base diameter faster than the droplet on the silicon oxide (good

wetting surface). We use the cylinder model to simulate the dynamics of the water droplets and the truncated sphere model for the ink droplets. The images in Figure 3.9 confirm the validity of the truncated sphere model rather than the cylinder model, for ink droplets. The agreement between the predictions and the experimental data is very strong in each case.

Figure 3.10 illustrates the dynamic behavior exhibited by droplets of different liquids colliding with the same target surface. Although the Weber numbers of the impacting droplets are similar, the variation in the liquid properties causes a significant difference in the Reynolds number and the contact angle. We observe that the decrease in the Reynolds number reduces the spread factor in both Figure 3.10 (a) and (b). Furthermore, the recoiling is less pronounced when wetting is improved (see the equilibrium contact angles in Appendix E). In all cases, the models predict the experimental results very closely. Images of a silicone oil droplet colliding with an acrylic surface are shown in Figure 3.11. After the silicone oil droplet recoils to form a relatively tall truncated sphere, it spreads to a very thin film since its equilibrium contact angle with the acrylic is very small.

Having investigated the effects of impact conditions on the post-impact oscillations, we examine the individual effect of impact conditions such as the Weber number, the Reynolds number, and the contact angle on the droplet dynamics, through theoretical modeling. Figures 3.12 (a) and (b) show the effects of the Weber number and the Reynolds number, respectively, on the temporal evolution of the base diameter. These graphs use the contact angle between a water droplet and acrylic surface. We use the cylinder model which has been proven to best fit the experimental data for water droplets on acrylic. Although a higher Weber number and a higher Reynolds number both increase the spread factor, the recoiling processes show different features. With the same Reynolds number, droplets with a low Weber number recoil faster and require less time to return to the equilibrium base diameter (Figure 3.12 (a)). On the other hand, when the Weber number remains constant, droplets with a higher Reynolds number recoil faster than those with low Reynolds number (Figure 3.12 (b)). Figure 3.12 (a) is explained as follows. A low Weber number implies that the relative magnitude of the surface energy to the initial impact energy is greater than high Weber number, and thus, this contributes to the faster recoiling which is a surface-energy dominated phenomenon. Furthermore, the increase in the degree of spreading due to the high Weber number, causes more viscous dissipation even at the same Reynolds number. This is because as the base area increases, more friction is experienced by the droplet on the target surface. The events depicted in Figure 3.12 (b) are explained as follows. Droplets with a high Reynolds

number experience less viscous dissipation. Therefore, droplets with higher Reynolds numbers recoil faster when the relative magnitude of the surface energy to the initial impact energy is the same.

The effect of contact angle on droplet oscillations is illustrated in Figure 3.13. We show the temporal evolution of the base diameter dependent upon the contact angle while keeping the Weber number and Reynolds number constant. As the contact angle decreases, the spread factor increases owing to the improved wetting. The recoiling process is fairly sensitive to the contact angle so that the droplets with higher contact angle (poor wetting) retract much faster than those with lower contact angle.

3.5. Discussions and conclusions

We have investigated the spreading and subsequent oscillations of various liquid droplets upon collision with different solid surfaces. In our experiments, sequential images of the impacting droplets are captured by a high speed video system. We analyze the images to obtain the temporal evolution of the base diameter of the droplet. To understand the physical phenomena, we develop a model based on the variational principle, assuming the droplet shape to be cylindrical. We also modify an existing variational model which assumes the droplet to be a truncated sphere.

Our experiments show that droplets with high impact inertia, associated with high We and Re, oscillate more vigorously upon collision with the solid surface. The oscillation is greatly affected by the wetting between the liquid droplet and the solid surface. Good wetting weakens and slows down the recoiling process. Moreover, experiments using droplets of different liquids and the same target solid show the strong effects of liquid properties and wetting behavior on the oscillation phenomena. Modeling results are in good agreement with the experimental data, demonstrating the capability of our models to predict the complicated phenomena of the droplet spreading and recoiling. In addition, the individual effects of parameters such as We, Re, and the contact angle are examined by using our model. The analysis shows that surface energy and viscous dissipation play critical roles in determining droplet dynamics. It is also shown through the model that the droplet dynamics are strongly affected by the contact angle, thus, poor wetting greatly promotes the recoiling.

When the recoiling of the liquid droplet is vigorous, we may even observe a necking of the liquid column moving upward, as shown in Figure 3.14. Similar phenomena were observed by Wachters and Westerling (1966) and Chandra and Avedisian (1991). Their observations were made on liquid drops impacting heated

targets above the boiling temperature of the liquid. It is also interesting to note that Chandra and Avedisian observed a very different recoiling process for different target temperatures. According to their measurement, the contact angle strongly depends on the target temperature. Therefore, the droplets hitting hot surfaces with a large contact angle recoil very vigorously while the droplets do not exhibit such recoiling on cold surfaces with small contact angle. This is consistent with our experimental observations.

In both the cylinder and the truncated sphere models, it is necessary to determine the dissipation factor, F_d. We have determined the values such that the modeling results best fit the experimental data. Although the method is purely empirical, we find that the values are constant for each liquid and for each model regardless of the target material. Table 3.2 summarizes the values of F_d used in our simulation.

Our models using the variational principle predict the experimental data surprisingly well, considering their approximate nature. A significant computational effort is saved by solving a single second-order, nonlinear differential equation instead of solving the full Navier-Stokes equation with the moving boundary. Furthermore, our study shows that by using the equilibrium contact angle, the experimental measurements can be predicted very closely. However, we find room where the dynamic contact angles may improve the prediction accuracy. The effect of the dynamic contact angles is well pronounced especially in water droplets on acrylic. The measurements show that the base diameter remains for a finite time around the maximum spread diameter while our cylinder model predicts an immediate recoiling. In reality, the droplet spends more time than the model predicts before the recoiling starts due to the contact angle hysteresis. While the droplet reverses its direction of motion, the dynamic contact angle should change from the advancing angle to the receding angle. That is, the recoiling is delayed in reality since the contact line may stay at rest within a range of contact angles (contact angle hysteresis).

TABLE 3.1. Physical properties of the liquids used in the experiments.

Liquid	Density (kg/m^3)	Surface tension (N/m)	Viscosity ($kg/(m \cdot s)$)
Water	996	0.0717	8.67×10^{-4}
Ink	1052	0.055	2.6×10^{-3}
Silicone oil	1064	0.0373	3.63×10^{-2}

TABLE 3.2. Dissipation factors.

Liquid	Assumed shape in model	F_d
Water	Cylinder	15
Water	Truncated sphere	5.3
Ink	Truncated sphere	3.2
Silicone oil	Truncated sphere	3.2

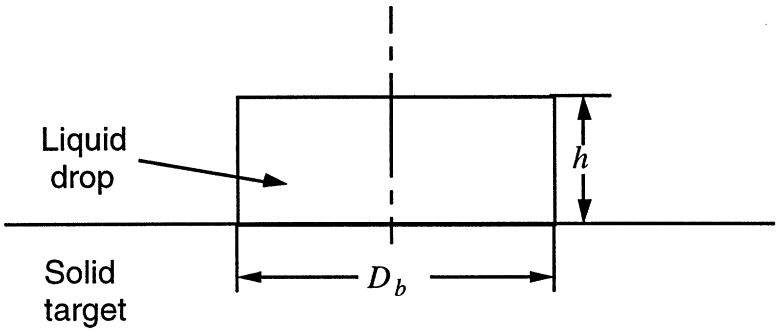

FIGURE 3.1. Geometry of the cylinder model.

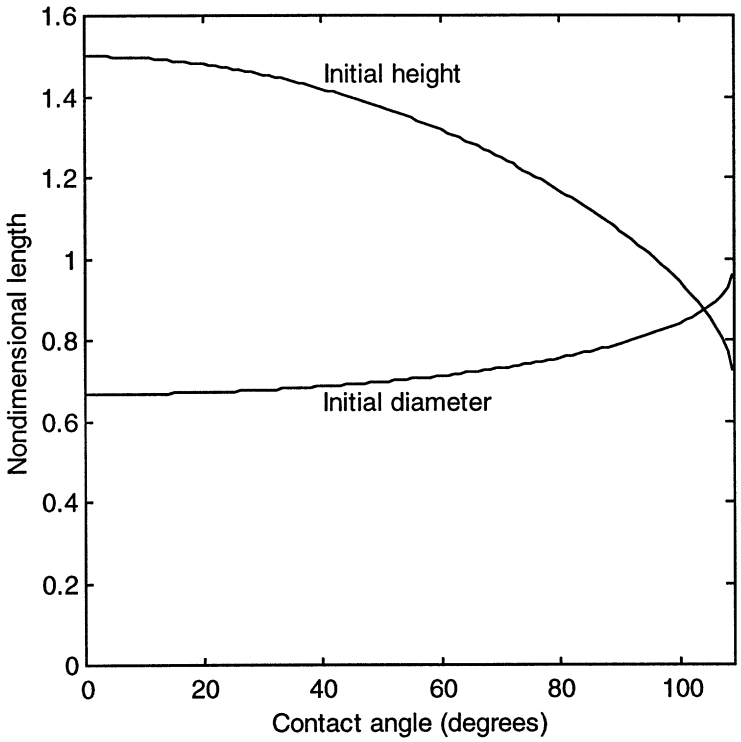

FIGURE 3.2. Initial diameter and height of the cylinder versus contact angle as given by Eq. (3.24) and (3.4).

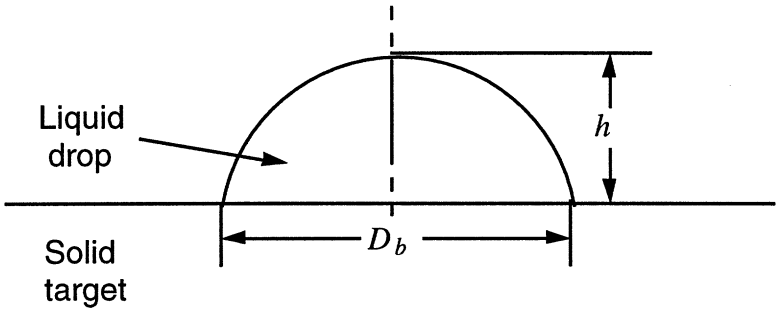

FIGURE 3.3. Geometry of the truncated sphere model.

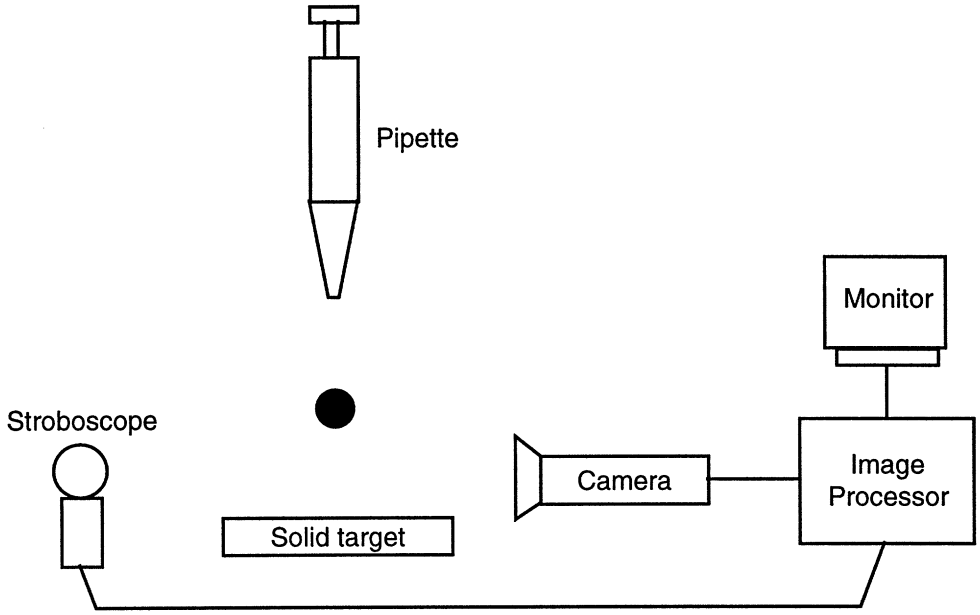

FIGURE 3.4. Experimental apparatus for the high speed imaging of droplet oscillations.

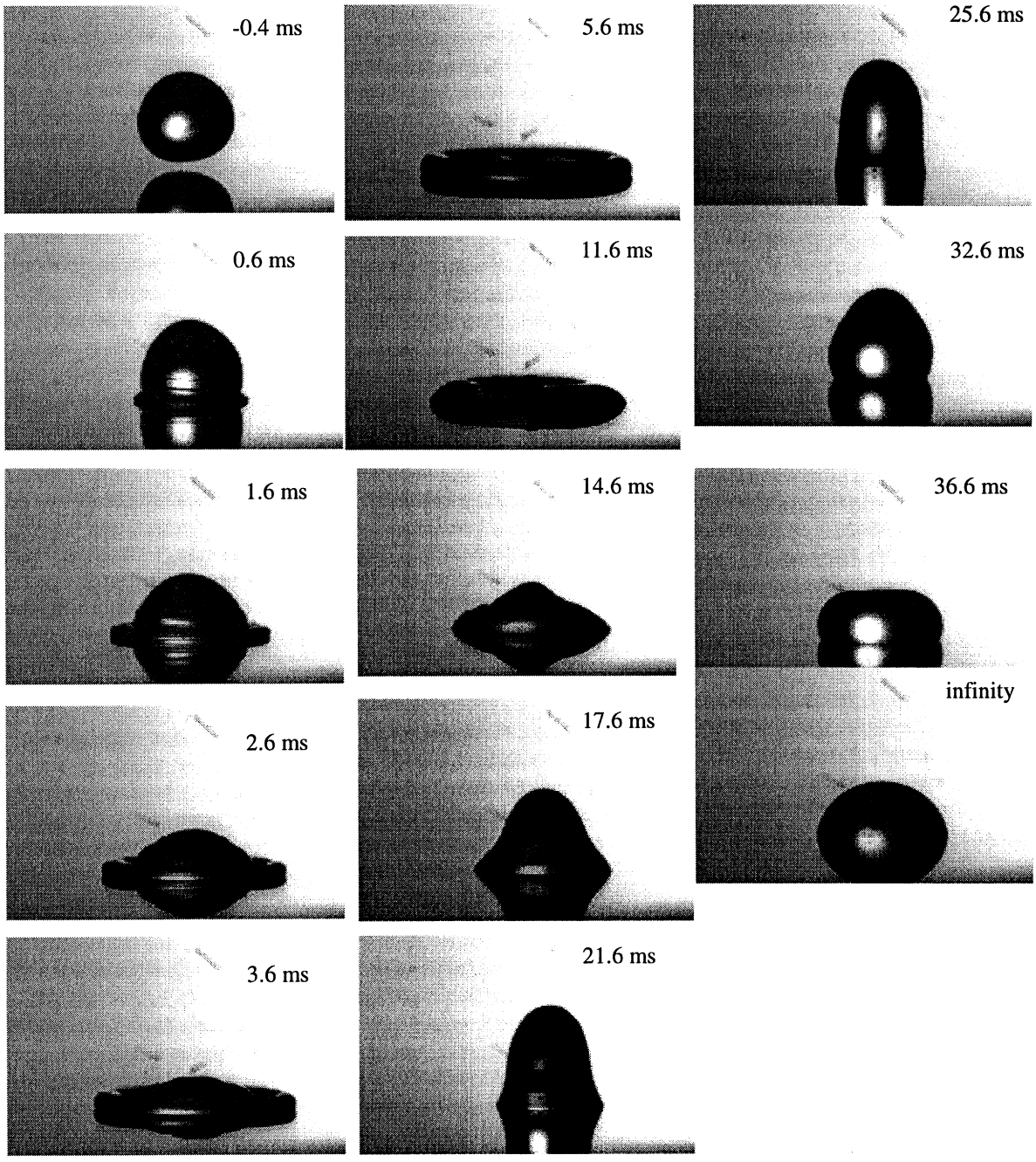

(a)

FIGURE 3.5. *continued in the next page*

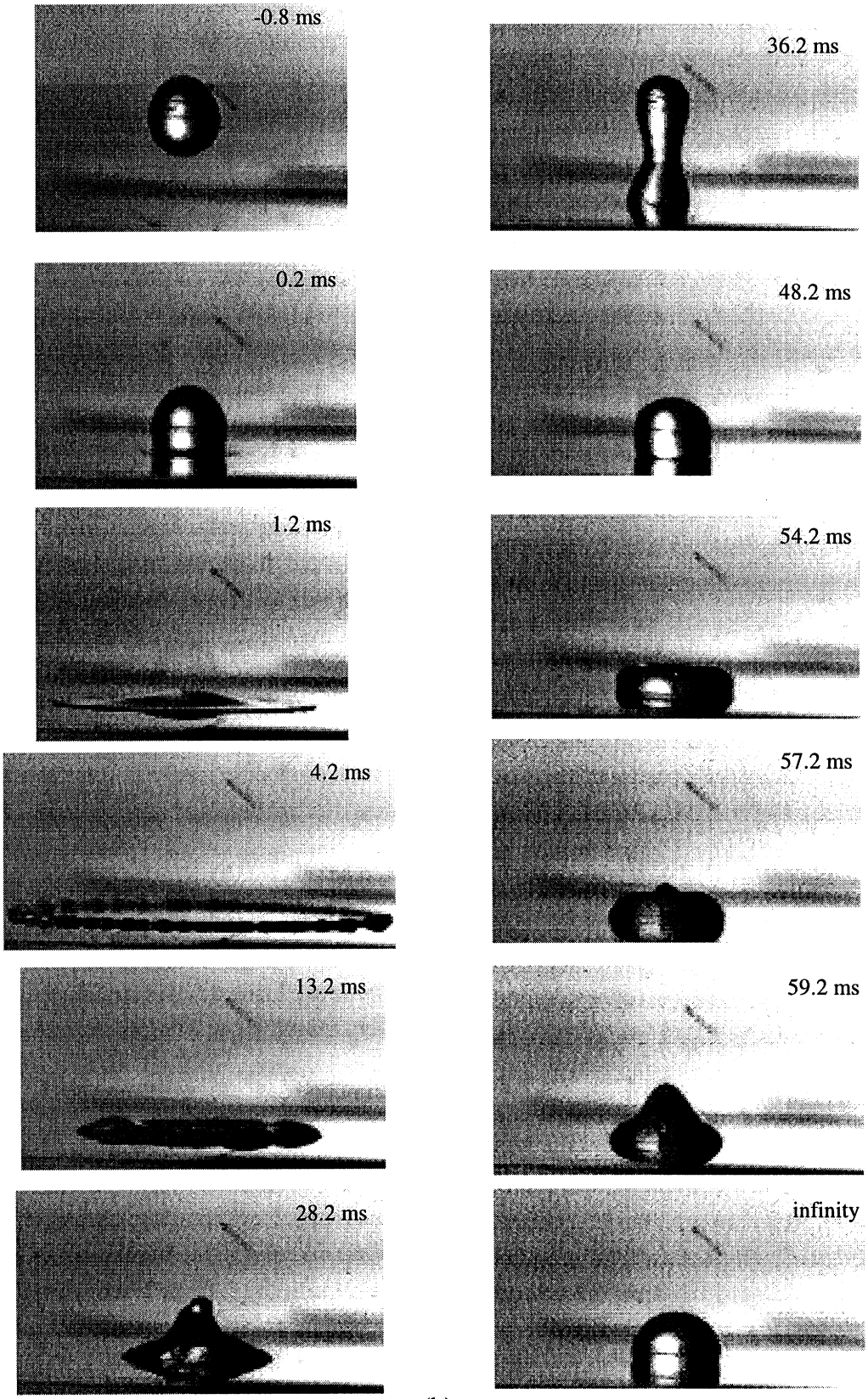
-0.8 ms
36.2 ms
0.2 ms
48.2 ms
1.2 ms
54.2 ms
4.2 ms
57.2 ms
13.2 ms
59.2 ms
28.2 ms
infinity

(b)

continued from the previous page

FIGURE 3.5. Images of a water droplet colliding with acrylic surface. (a) Original droplet diameter = 3.6 mm, Impact velocity = 0.77 m/s, We = 30, Re = 3214. (b) Original droplet diameter = 3.5 mm, Impact velocity = 3.47 m/s, We = 582, Re = 13850.

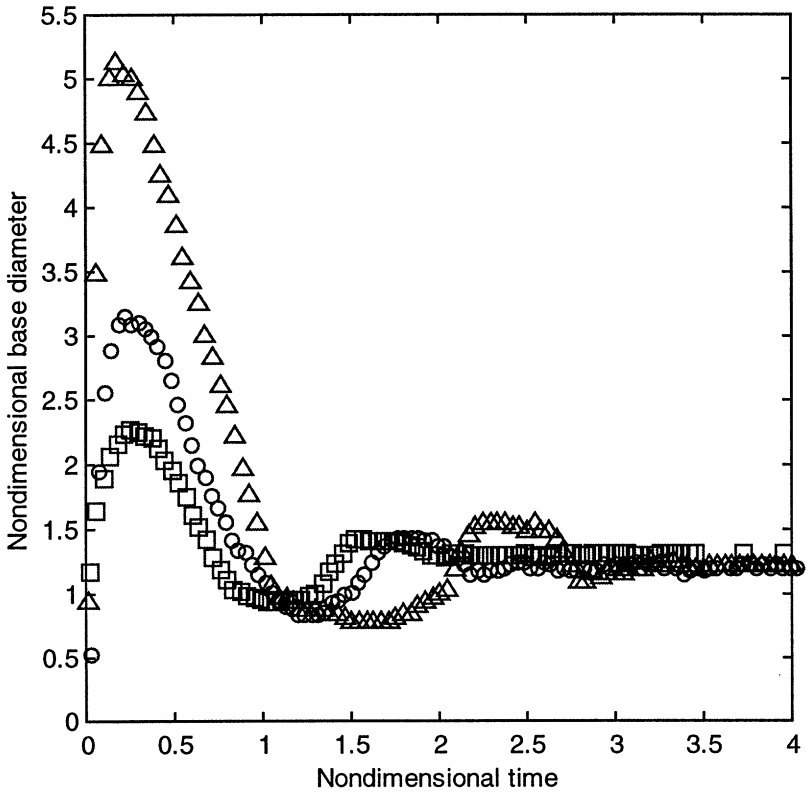

FIGURE 3.6. The temporal evolution of the base diameter of water droplets colliding with acrylic surface. The impact conditions for triangles and squares are the same as the Figure 3.5 (a) and (b), respectively. The impact conditions for circles: Original droplet diameter = 3.7 mm, Impact velocity = 1.63 m/s, We = 137, Re = 6950.

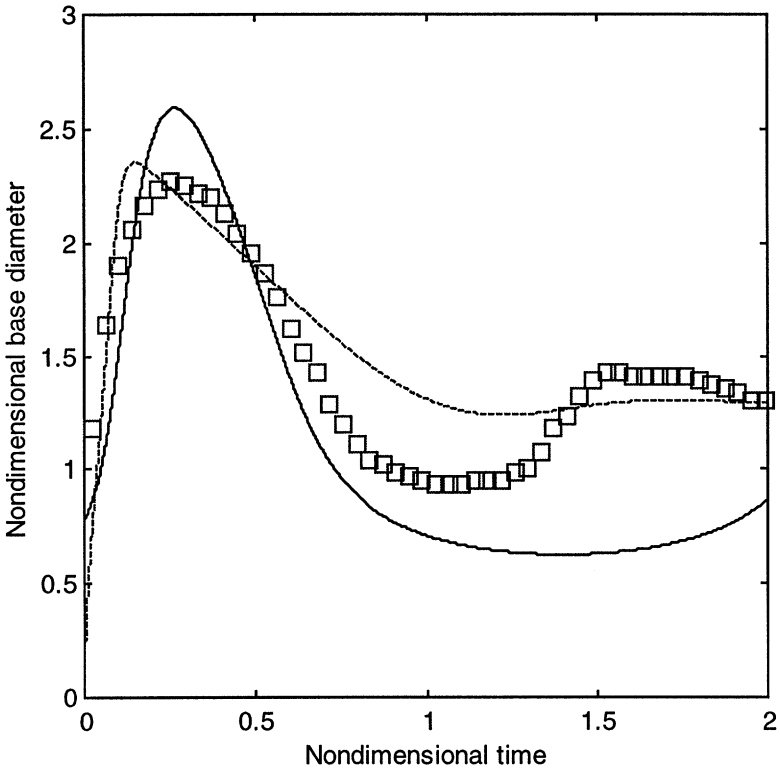
Nondimensional base diameter
Nondimensional time
0
0.5
1
1.5
2
2.5
3

(a)

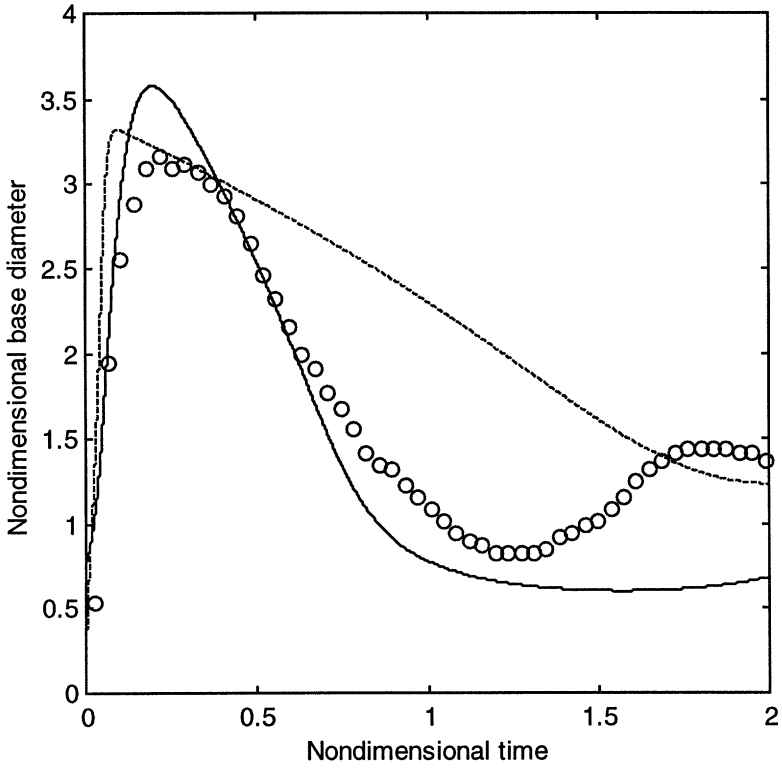
Nondimensional base diameter
Nondimensional time
0
0.5
1
1.5
2
2.5
3
3.5
4

(b)

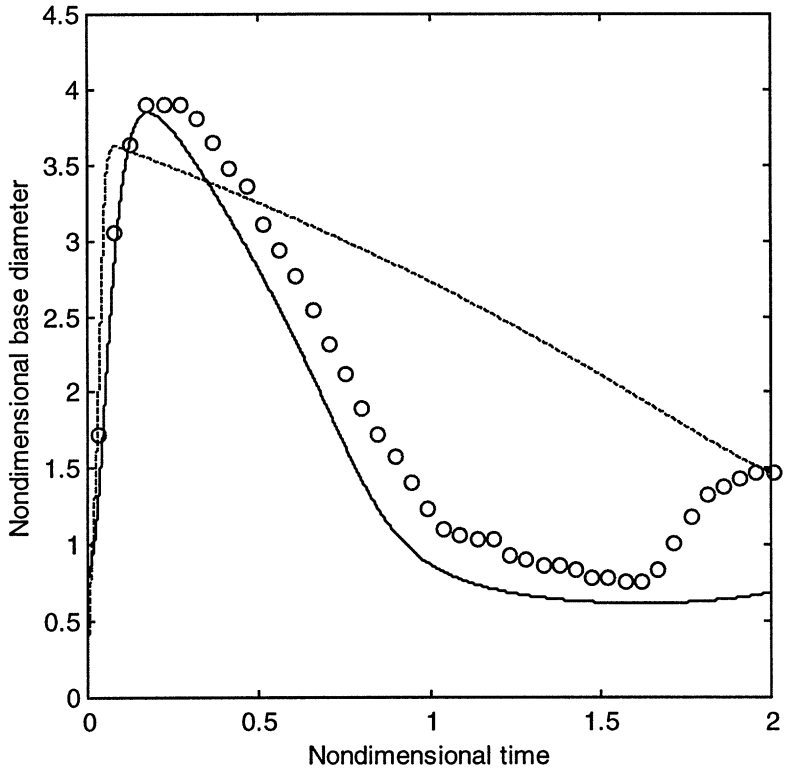

(c)

FIGURE 3.7. Predictions of the models and the experimental measurements for water droplets on acrylic surface. Modeling results using the cylinder model (solid line) and the truncated sphere model (broken line) are both presented. (a) We = 30, Re = 3210. (b) We = 137, Re = 6950, (c) We = 207, Re = 7850.

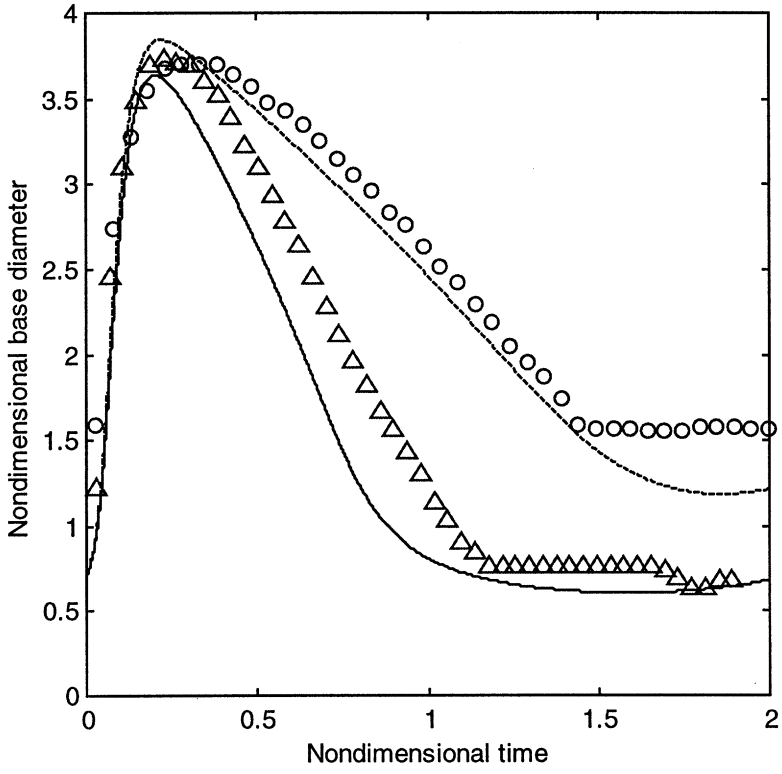

(a)

FIGURE 3.8. *continued in the next page*

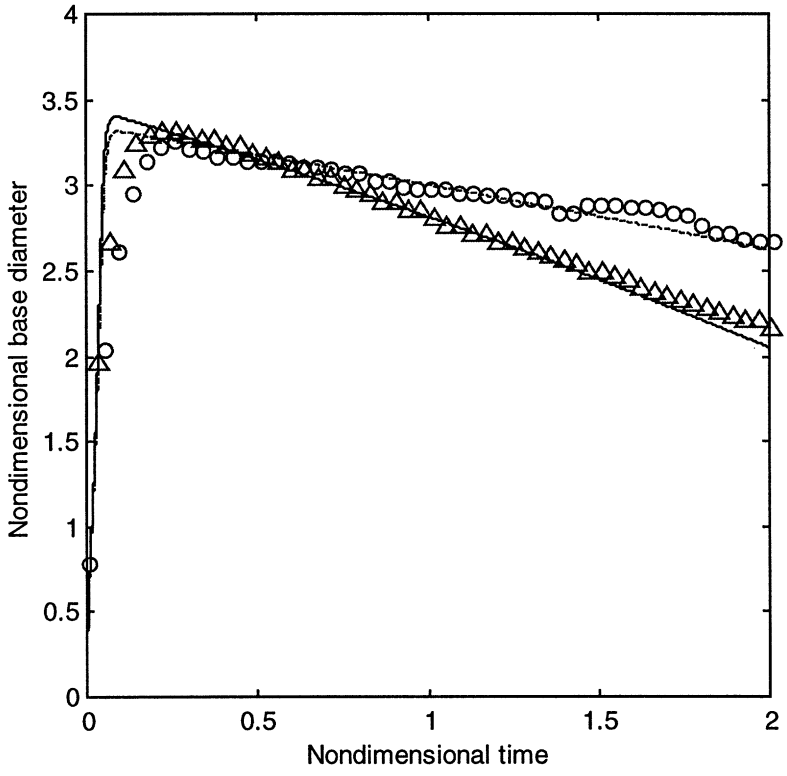

(b)

FIGURE 3.8. Effect of target surfaces on droplet dynamics. (a) Water droplet on acrylic (triangles and solid line: We = 150, Re = 7142) and silicon oxide (circles and broken line: We = 166, Re = 6938). (b) Ink droplet on acrylic (triangles and solid line: We = 190, Re = 2296) and silicon oxide (circles and broken line: We = 170, Re = 2127).

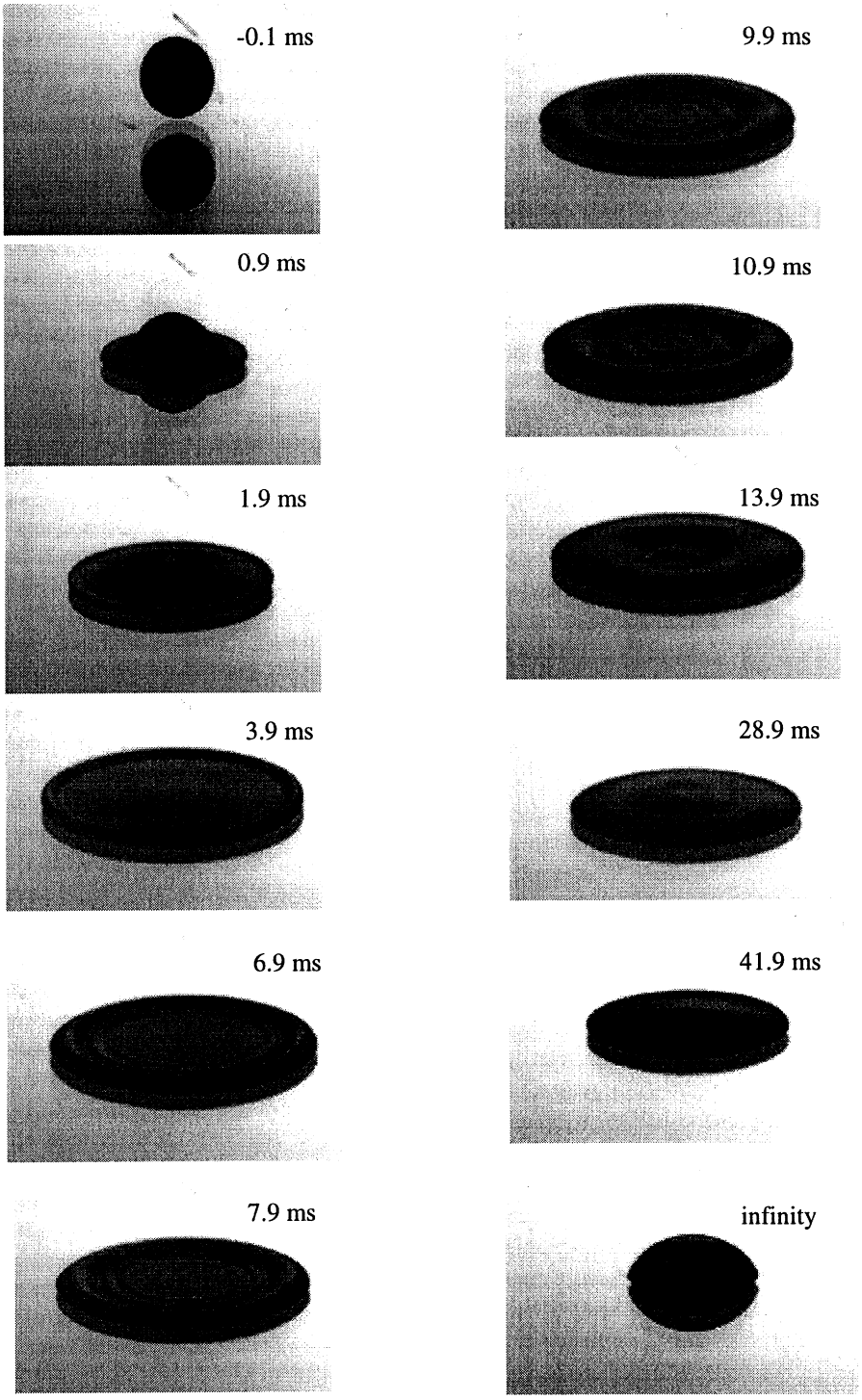

FIGURE 3.9. Images of an ink droplet colliding with acrylic surface. Original droplet diameter = 3.2 mm, Impact velocity = 1.75 m/s, We = 190, Re = 2296.

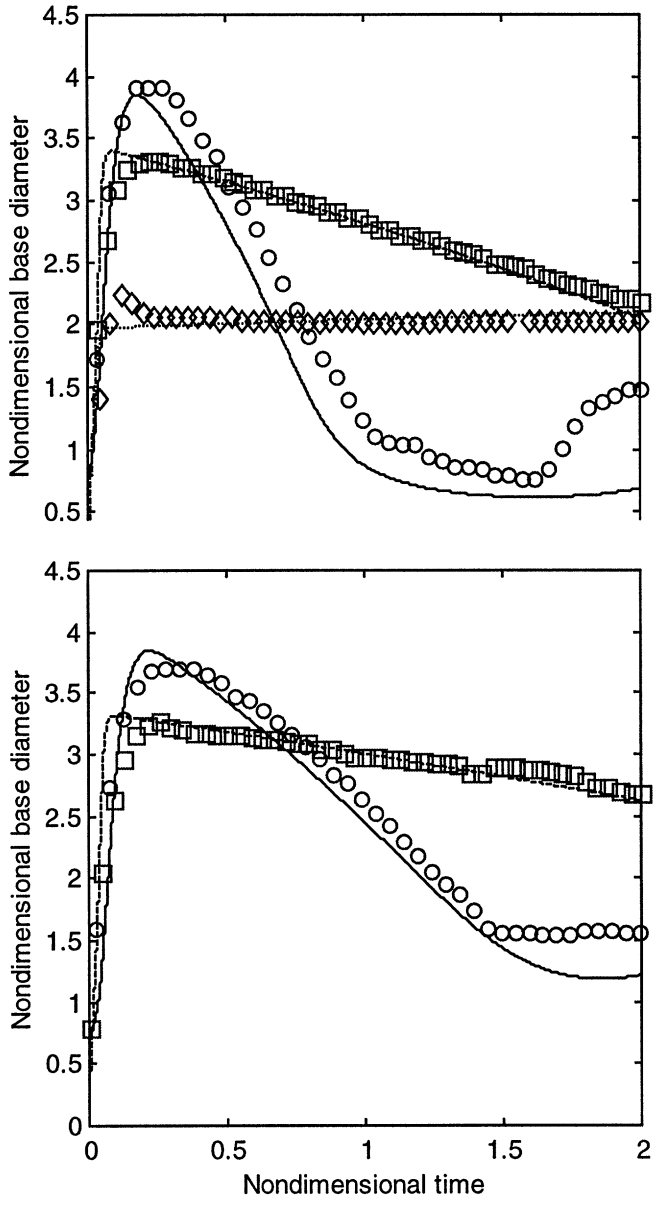

FIGURE 3.10. (a) Dynamic behavior of water (circles and solid line: We=207, Re = 7850), ink (squares and broken line: We =190, Re = 2296), and silicone oil (diamonds and dotted line: We =166, Re = 118) droplets colliding with the acrylic surface. (b) Dynamic behavior of water (circles and solid line: We = 166, Re = 6938) and ink (squares and broken line: We = 170, Re = 2127) droplets colliding with the silicon oxide surface.

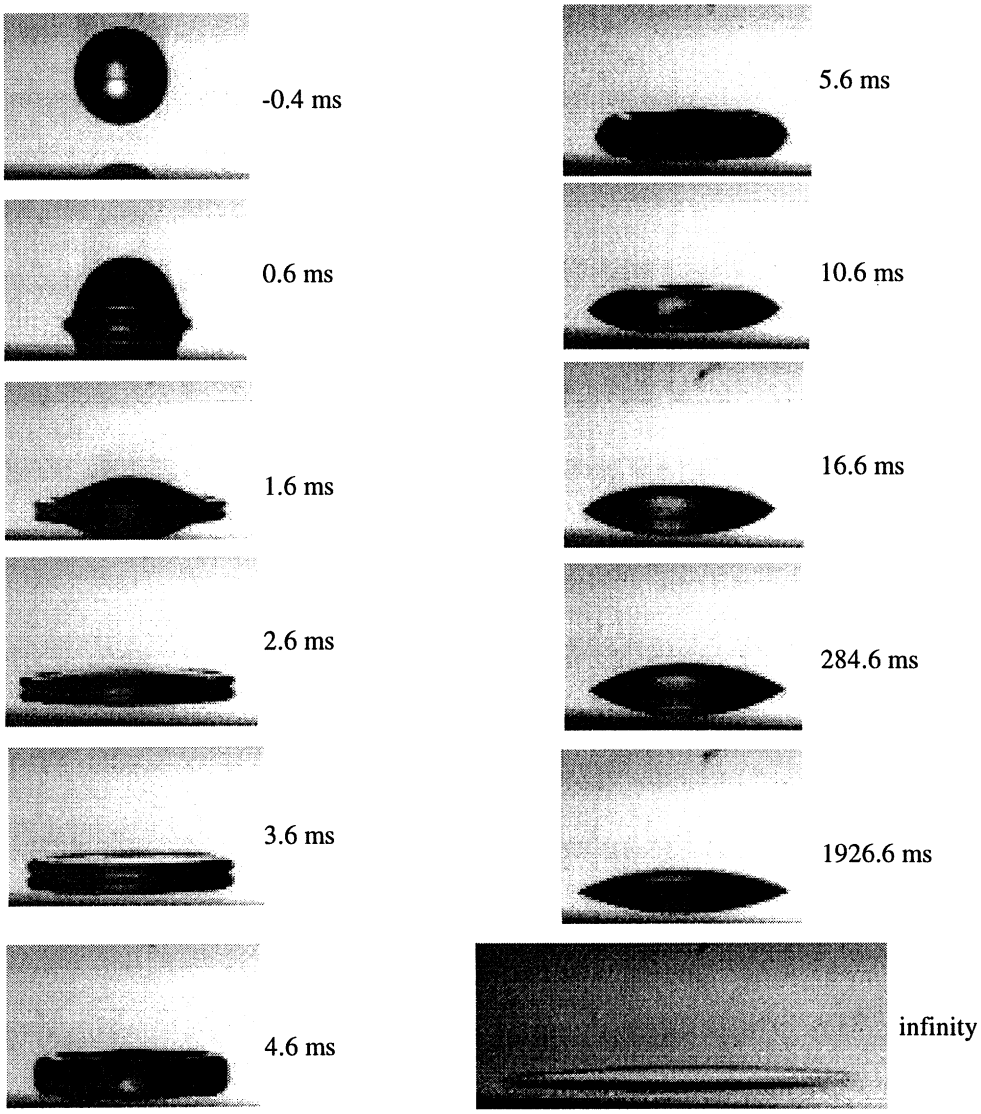

FIGURE 3.11. Images of a silicone oil droplet colliding with acrylic surface. Original droplet diameter = 2.8 mm, Impact velocity = 1.44 m/s, We = 166, Re = 118.

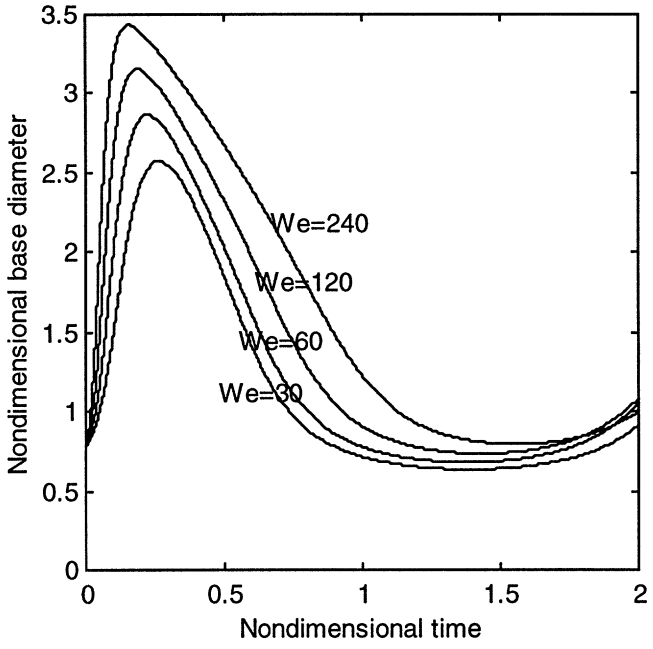

(a)

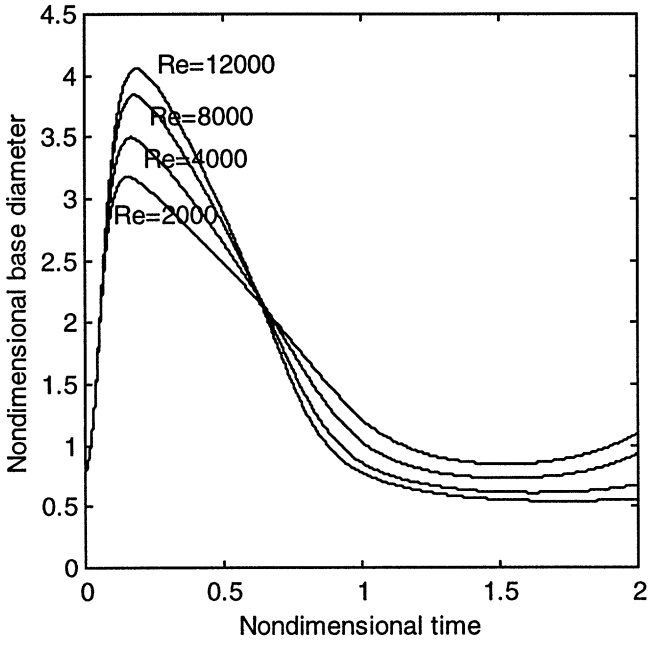

(b)

FIGURE 3.12. Effect of (a) the Weber number and (b) the Reynolds number on the dynamics of water droplets on the acrylic. The simulations are based on the cylinder model. (a) Re is fixed at 3000. (b) We is fixed at 200.

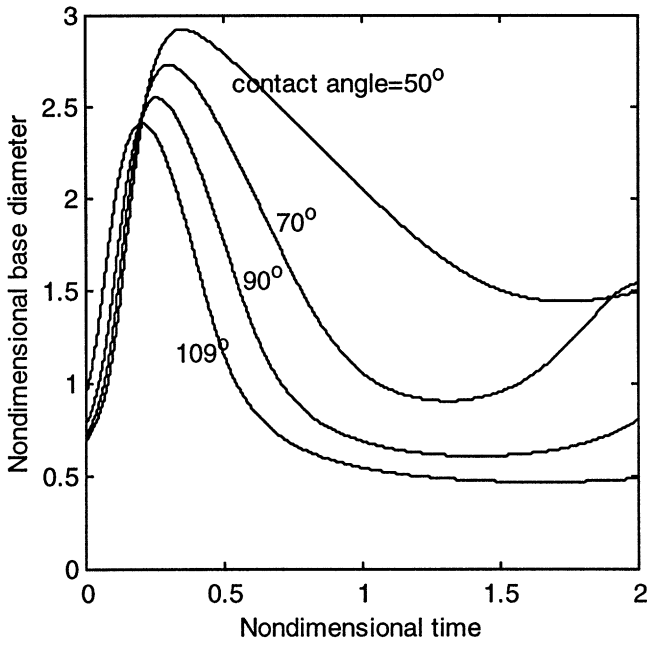

(a)

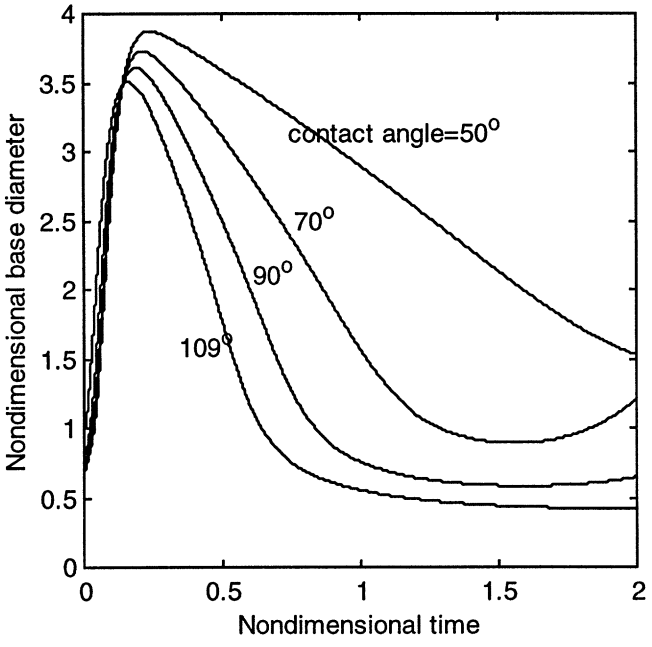

(b)

FIGURE 3.13. Effect of the contact angle on the droplet dynamics. The simulations are based on the cylinder model. (a) We = 30 and Re = 3000. (b) We = 150 and Re = 7000.

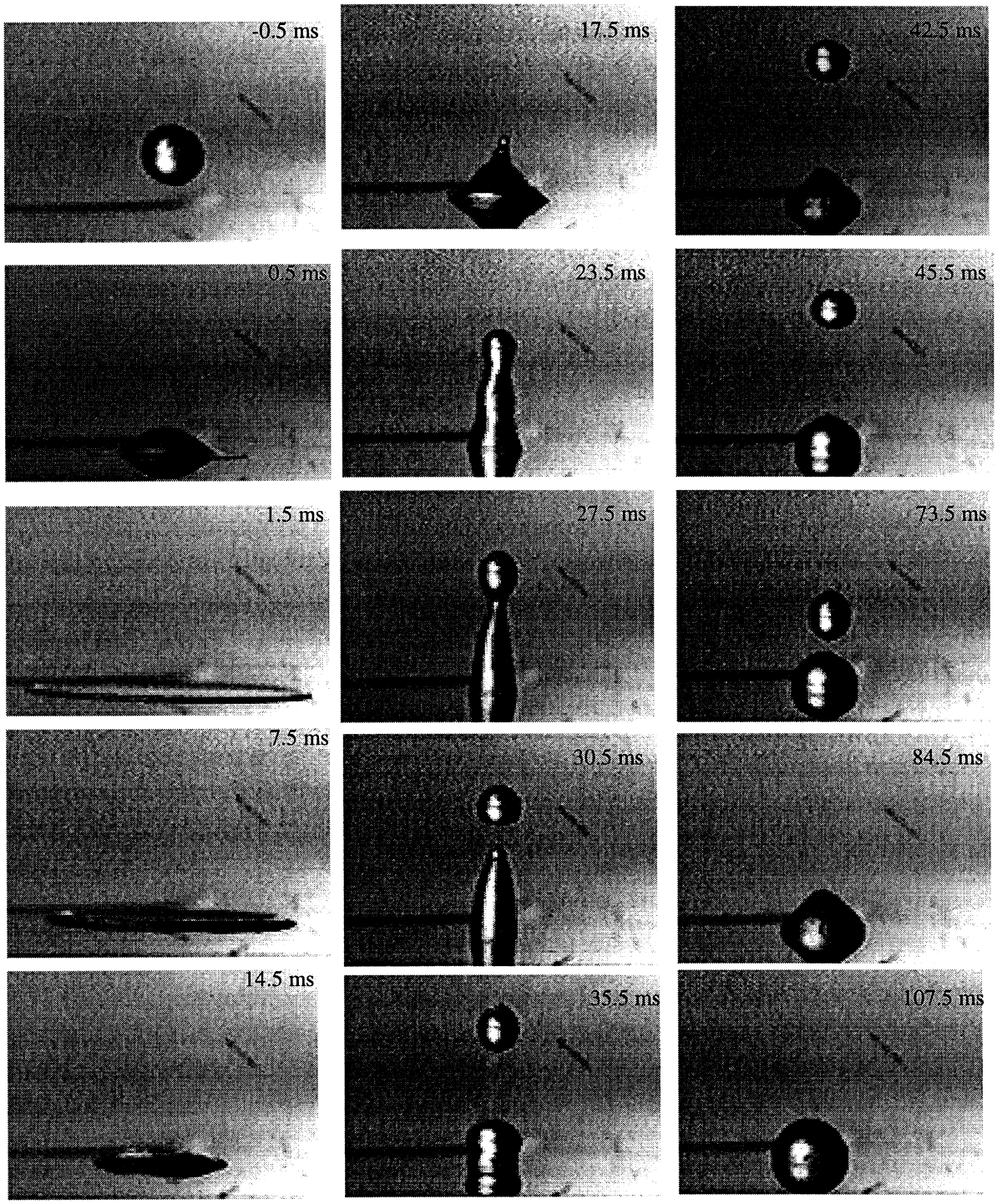

FIGURE 3.14. Necking of a rising water column during a recoiling process. Original droplet diameter = 2.9 mm, Impact velocity = 3.57 m/s, We = 516, Re = 11890.

CHAPTER 4

BOUNCING OF MOLTEN METAL DROPLETS UPON COLLISION WITH SOLID SURFACES

4.1. Introduction

The spreading behavior of molten droplets has been the subject of intense study recently. Those studies mainly focus on the mechanism which arrests the motion of a droplet spreading on a subcooled target. However, our current study investigates a rather strange behavior of molten metal droplets. Under certain conditions, metal droplets do not stick to target surfaces but rather, they bounce off. Spreading and the subsequent arrest by solidification of molten droplets can occur only when bouncing is absent or prevented. Understanding of the bouncing phenomenon is especially important in electronic packaging where an individual solder droplet is deposited and its shape is critical for the quality of the connection (Waldvogel and Poulikakos 1997). In addition, since bouncing induces poor physical contact between the droplet and its target, the quality of spray-formed deposits is greatly affected by the phenomenon as well (Matson et al. 1998).

In this chapter, we examine the basic physics of the bouncing of molten metal droplets. We investigate the effects of both the dynamic and thermal conditions of the droplet impact on the bouncing. High speed imaging reveals that bouncing is a very violent form of droplet oscillation upon its collision with a solid surface. It is also observed that the bouncing is prevented when the base of the droplet freezes faster than recoiling can take place. Based on the observations, we develop a simple model leading to a regime map which divides the bouncing and sticking regions based on thermal and dynamic conditions.

4.2. Description of the experimental apparatus

Pure tin is used as the droplet material. We employ two different methods to investigate the bouncing of molten tin droplets. The first method is illustrated in Figure 4.1. Tin is melted in a stainless steel crucible. A thermocouple inserted in the crucible and a band heater wrapped around the crucible are connected to a controller to maintain a constant melt temperature. Molten material is ejected through an orifice, 100 μm in diameter, by the introduction of high pressure nitrogen gas into the crucible. When initiating the

ejection of molten material, a certain pressure difference needs to be established and a jet is always formed instead of drops. After establishing the jet, we rapidly relieve the pressure inside the crucible to produce molten material in the form of a droplet. The diameter range of the droplets generated by such means, is from approximately 1.3 mm to 2.7 mm. The molten droplet falls onto a solid target surface located 0.43 m below the orifice. As the target solids, pure copper, 6061 aluminum alloy, pure tin, silicon bronze, 304 stainless steel, and plane glass are used. All the surfaces are polished with a 1-μm diamond paste except the glass surface. The surface is heated underneath by an aluminum block in which a cartridge heater is inserted. The surface temperature is measured by a miniature thermocouple tightly pressed onto the surface. The temperature varies from room temperature to near the melting temperature of the droplet material (232°C for pure tin). Droplets are generated and deposited in a chamber which is constantly flushed with positive gauge pressure (34 kPa) of nitrogen gas to prevent oxidation.

A high speed video system (Kodak Ektapro EM, Model 1012) records the dynamic behavior of a droplet upon colliding with a subcooled surface at a rate of 1000 frames per second. An image stored in the system consists of 192 X 239 pixels. The illumination is provided by a stroboscope which is synchronized with the camera, thus, very sharp images are captured. The images stored in the digital memory are downloaded onto a video tape using a S-VHS video tape recorder, and analyzed by an image analysis software which is capable of measuring the dimensions of objects by the number of pixels. An object of a known size (8 mm in diameter) is recorded by the same video setup and used for calibration.

While the above method produces millimeter-sized droplets, another method is used to generate droplets with a diameter on the order of 100 μm. The second method utilizes the uniform droplet spray process to produce microdroplets of a uniform size, velocity, and temperature. The description of the droplet generation process is presented elsewhere (Yim et al. 1996). Because the currently available imaging system is unable to capture a phenomenon as fast as the impact of microdroplets, we observe the final shapes of splats collected on solid surfaces. The surfaces of the same materials used above, are heated in the same manner as described in the first method. The experiments are also performed in a nitrogen-flushed atmosphere. The schematic of the method is illustrated in Figure 4.2.

4.3. Results and discussion

4.3.1. *Experimental observations*

We first compare images of droplets colliding with solid surfaces of different thermal states, as shown in Figure 4.3. The fringe of the droplet in Figure 4.3 (a) is arrested due to solidification at approximately 2.9 ms after impact while the rest of molten volume recoils back to the center until it completely freezes. On the other hand, the droplet in Figure 4.3 (b) shows a very vigorous oscillation upon colliding with the target, due to the absence of solidification. The strong oscillation brings the droplet back to its original spherical shape while lifting it into the air. In other words, an image in Figure 4.3 (b), at 17.6 ms after impact, looks like an elastic solid ball bouncing off a solid wall. Figure 4.3 (c) shows a transitional phenomenon between (a) and (b): although the recoiling of the droplet is more pronounced and lasts longer than (a), the droplet fails to disengage from the surface due to freezing.

Next, we investigate the effect of droplet size on bouncing, which is well pronounced in the impact of microdroplets. The small droplet of Figure 4.4 (a) bounces and creates a highly irregular splat, while the large droplet of Figure 4.4 (b) forms a regular splat shape due to freezing before bouncing. This result indicates that the role of droplet size should be considered in addition to the thermal aspects to fully describe bouncing behavior.

Our experimental study showed that droplets bounce upon collision with hot surfaces of all target materials except tin. Figure 4.5 shows the very different behavior of molten tin droplets upon colliding with a tin target. Although the dynamic and thermal states of the droplet and the target satisfy the conditions for bouncing (see below), the droplet does not bounce off the target of its own material. We note that any liquid wets a solid of the same material. Therefore, this result implies that good wetting between the droplet and the target surface prevents bouncing.

The experimental observations described so far provide the basic features of the bouncing of molten metal droplets. The following section develops an approximate model which quantifies criteria to determine whether the droplet bounces off or sticks to the target surface.

4.3.2. *An approximate model*

As observed above, molten tin droplets tend to bounce off solid surfaces when oscillating violently upon colliding with nonwetting surfaces in the absence of solidification. If the heat loss to the subcooled target surface is significant, solidification arrests the recoiling front of the droplet, preventing it from bouncing. In addition, under certain thermal conditions, only small droplets, which have a short oscillation time, bounce while the larger ones do not. Based on these experimental observations, we assume that the bouncing of molten droplets is dependent upon the relative magnitudes of the oscillation and solidification times in nonwetting conditions.

The period of the free oscillation of a liquid drop is used as the oscillation time scale. Therefore, our oscillation time, t_{osc}, is written as

$$t_{osc} = \left(\frac{\rho D^3}{\sigma} \right)^{1/2}. \tag{4.1}$$

We note that the kinetic energy of the impacting droplet affects the degree of bouncing. Schiaffino and Sonin (1997) observed a mercury droplet colliding with glass fully disengage from the surface when the Weber number exceeds 1.2. The Weber number is defined as $\mathrm{We} = \rho U^2 R/\sigma$, where ρ denotes the density, U the impact velocity, R the radius, and σ the surface tension of the droplet. When the Weber number is smaller than 1.2, the droplet does not completely detach from the surface. We assume that the tin droplets have a similar Weber number to that of mercury for the disengagement threshold. Since the Weber number of the droplets used in our experiments is well above unity, the bouncing always occurs in the nonwetting condition when solidification is absent.

The solidification time is estimated by considering one dimensional heat conduction from a molten droplet to a subcooled target solid. Carslaw and Jaeger (1959) offered the analytical solution to the problem in which two semi-infinite bodies of different temperature are in perfect contact while one of them undergoes solidification. The solution considers the superheat of the molten state and is able to obtain the exact thermal profile inside a solidifying layer. We apply this model to obtain the approximate solidification time of a droplet on a solid surface: the schematic of the problem is illustrated in Figure 4.6. In the following, subscripts *1* and *2* denote target solid and droplet, respectively, and superscripts *s* and *l* denote solid and liquid phase, respectively.

The thickness of a solidifying layer, $s(t)$ is given by

$$s(t) = 2\xi\left(\alpha_2^s t\right)^{1/2}, \tag{4.2}$$

where α_2^s is the thermal diffusivity of the solid state of the droplet, and t the time. A parameter ξ is determined from the solution of the following:

$$\frac{exp\left(-\xi^2\right)}{\mathrm{erf}(\xi)} + \frac{k_2^l}{k_2^s}\frac{\alpha_2^l}{\alpha_2^s}\frac{T_2^m - T_2^i}{T_2^m - T_{int}} \cdot \frac{\exp\left(-\xi^2\alpha_2^s/\alpha_2^l\right)}{\mathrm{erfc}\left[\xi\left(\alpha_1^s/\alpha_1^l\right)^{1/2}\right]} = \frac{\xi L_2 \pi^{1/2}}{c_2^s\left(T_2^m - T_{int}\right)}. \tag{4.3}$$

Furthermore, the interface temperature T_{int} is obtained by using the following:

$$T_{int} = \frac{T_2^m b_2^s + T_1^i b_1 \mathrm{erf}(\xi)}{b_2^s + b_1 \mathrm{erf}(\xi)}, \tag{4.4}$$

where the effusivity, b, is defined as $b = (k\rho c)^{1/2}$, in which k, ρ, and c are the thermal conductivity, density, and specific heat, respectively. The solidification time is obtained by Eq. (4.2) after specifying the solidifying layer thickness, s. Since we are interested in solidification which hinders motion at the droplet fringe before bouncing, our characteristic solidification thickness is assumed to scale as the hydrodynamic boundary layer thickness. The boundary layer thickness, δ_H, is estimated by modeling the flow as one on an oscillating wall with the period t_{osc} (Batchelor, 1967):

$$\delta_H = \left(\frac{\mu^2 D^3}{\rho\sigma}\right)^{1/4}. \tag{4.5}$$

Therefore, our solidification time, t_{sol}, is written as

$$t_{sol} = \left(\frac{1}{4\alpha_2^s \xi^2}\right)\delta_H^2. \tag{4.6}$$

We predict that when the solidification time is longer than the oscillation time, the droplet will bounce before its bottom is arrested. In the reverse case, the droplet will freeze at its bottom and so fail to disengage from the target.

4.3.3. *Regime map of droplet bouncing*

In this section, we provide experimental data on bouncing behavior obtained by varying the dynamic and thermal conditions of droplets and target surfaces. The data are interpreted using the model presented above. We calculate the oscillation and solidification times for each experimental condition and predict whether the droplets will bounce or stick. It is noted that our primary goal is to identify a trend which can be explained in the frame of our model.

Squares and circles in Figure 4.7 show the data collected by using nonwetting target surfaces. As predicted, when the oscillation time is short compared to the solidification time (lower right portion of the graph), the droplets bounce off the target (squares). On the other hand, the droplets stick to the target when the oscillation time is long compared to the solidification time (circles). Seeking an approximate threshold which determines the bounce of a droplet, we draw a line to separate the bouncing and sticking regions.

Pentagrams in Figure 4.7 shows the experimental results obtained by depositing molten tin droplets on solid tin targets. The droplets stick to the target even when the solidification time is much greater than the threshold value. This phenomenon is caused by the strong wetting between the droplet and the target surface. Based on this observation, we find that the wetting or contact angle is an additional parameter which affects the bouncing and sticking behavior of molten droplets. It appears that we can construct a regime map for bouncing and sticking using three independent parameters: the solidification time, the oscillation time, and the contact angle. However, we do not exclude the possibility that the contact angle should play only a minor role such that there is a threshold value under which strong wetting arrests the recoiling (as tin droplet on tin target in our study) and over which bouncing is not greatly affected. Further research to quantitatively assess the effects of wetting is strongly recommended.

4.4. Conclusions

In this chapter, the fundamentals of the bouncing behavior of molten metal droplets were studied using experiments and an approximate model. Two experimental methods were adopted. One uses molten tin droplets of millimeter size generated by slow ejection of molten material. Images of droplets bouncing or sticking upon colliding with various target conditions are recorded using a high speed video system. The other method utilizes the uniform droplet spray process to generate microdroplets and observation of the final splat shapes as collected on various target conditions, is carried out.

We interpret the experimental data based on the following assumption: whether the droplet will bounce or stick is determined by the competition between the relative magnitudes of the oscillation and solidification times. We scale the oscillation time to the oscillation period of a free liquid droplet. The solidification time is assumed to be the time it takes for the hydrodynamic boundary layer to solidify. The heat transfer from the droplet to the target is modeled by the heat conduction between two semi-infinite bodies, one of which undergoes solidification.

An empirical regime map is constructed based on the two time scales discussed above. We find a clear trend that the bouncing occurs when the solidification is slow compared to the oscillation, while the sticking occurs when the solidification is fast. Our experimental data suggest that there exist a threshold which determines whether the droplet will bounce or stick. We also find that bouncing is prohibited by good wetting between the droplet and the target. In other words, when the droplet and the target are of the same material, no bouncing is observed even when the solidification is fairly slow compared to the oscillation. This finding suggests the possible existence of a third independent parameter, wetting, that affects the bouncing behavior.

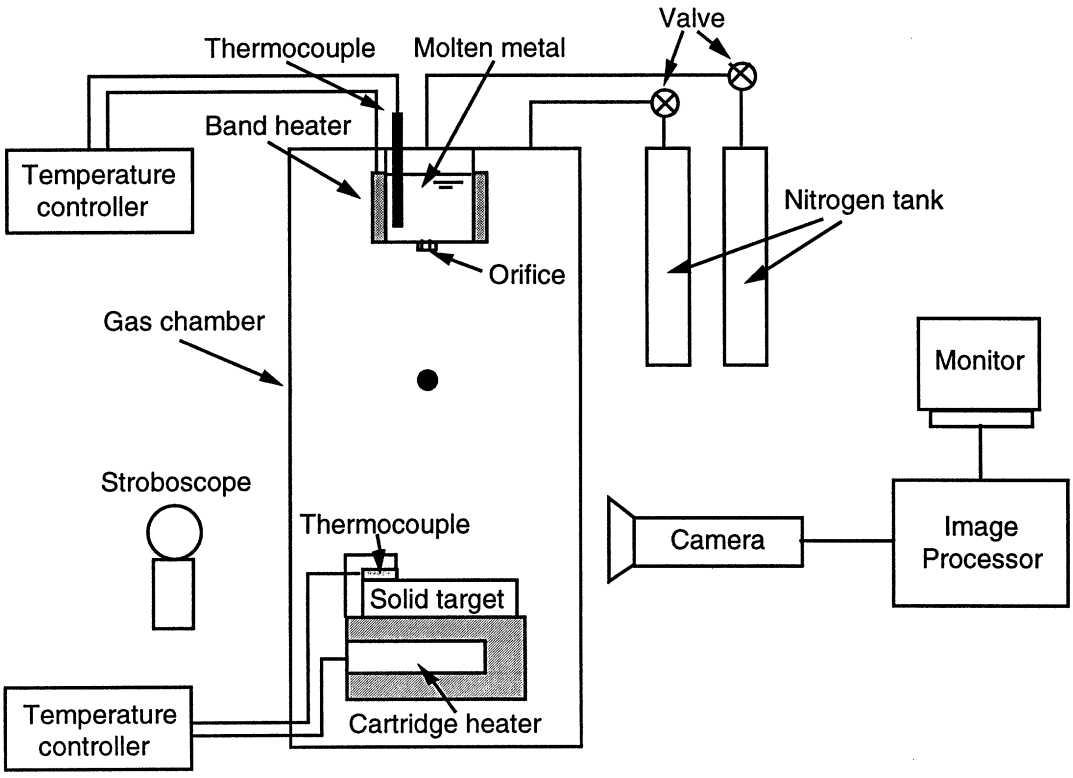

FIGURE 4.1. Experimental apparatus for the high speed imaging of millimeter-sized droplet impact.

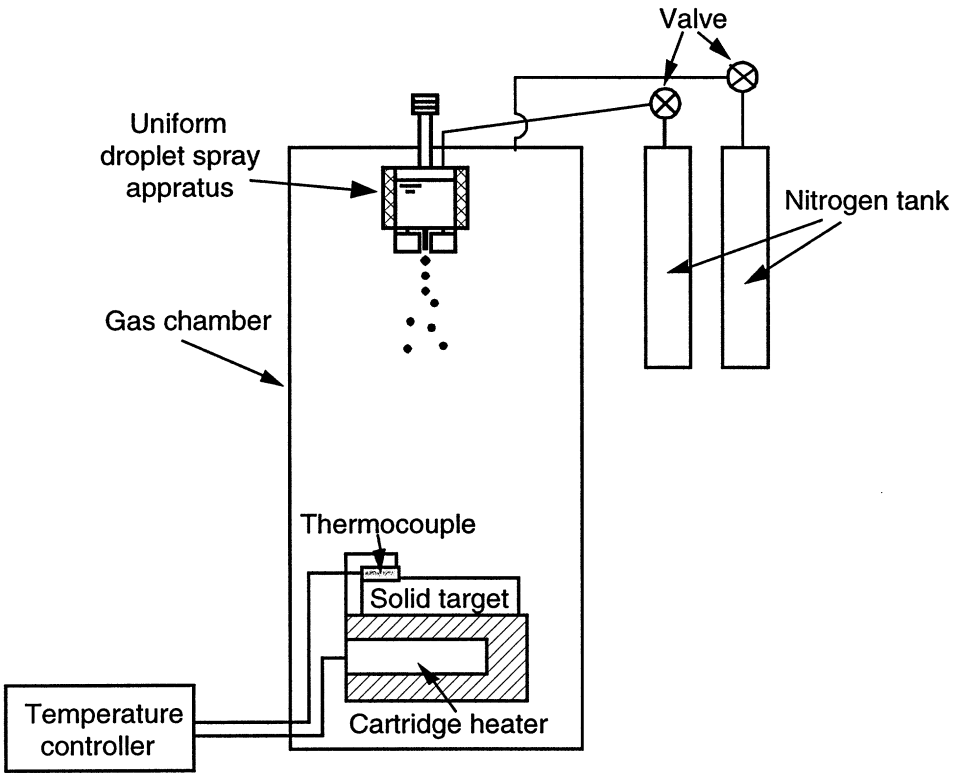

FIGURE 4.2. Experimental apparatus for the high speed imaging of microdroplet impact.

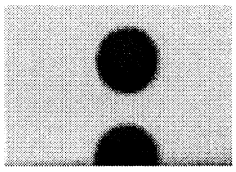
-0.1 ms

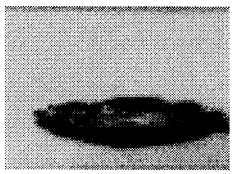
5.9 ms

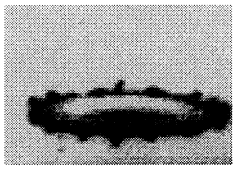
0.9 ms

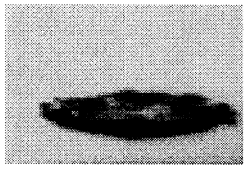
6.9 ms

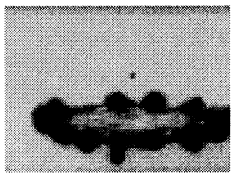
1.9 ms

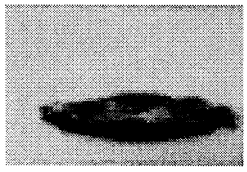
7.9 ms

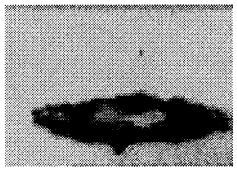
2.9 ms

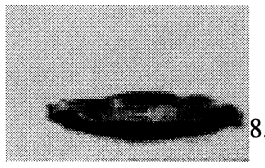
8.9 ms

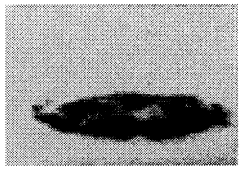
3.9 ms

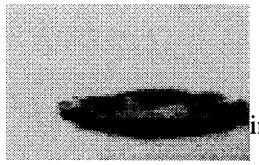
infinity

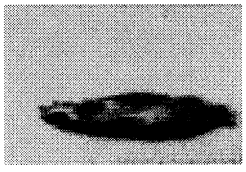
4.9 ms

(a)

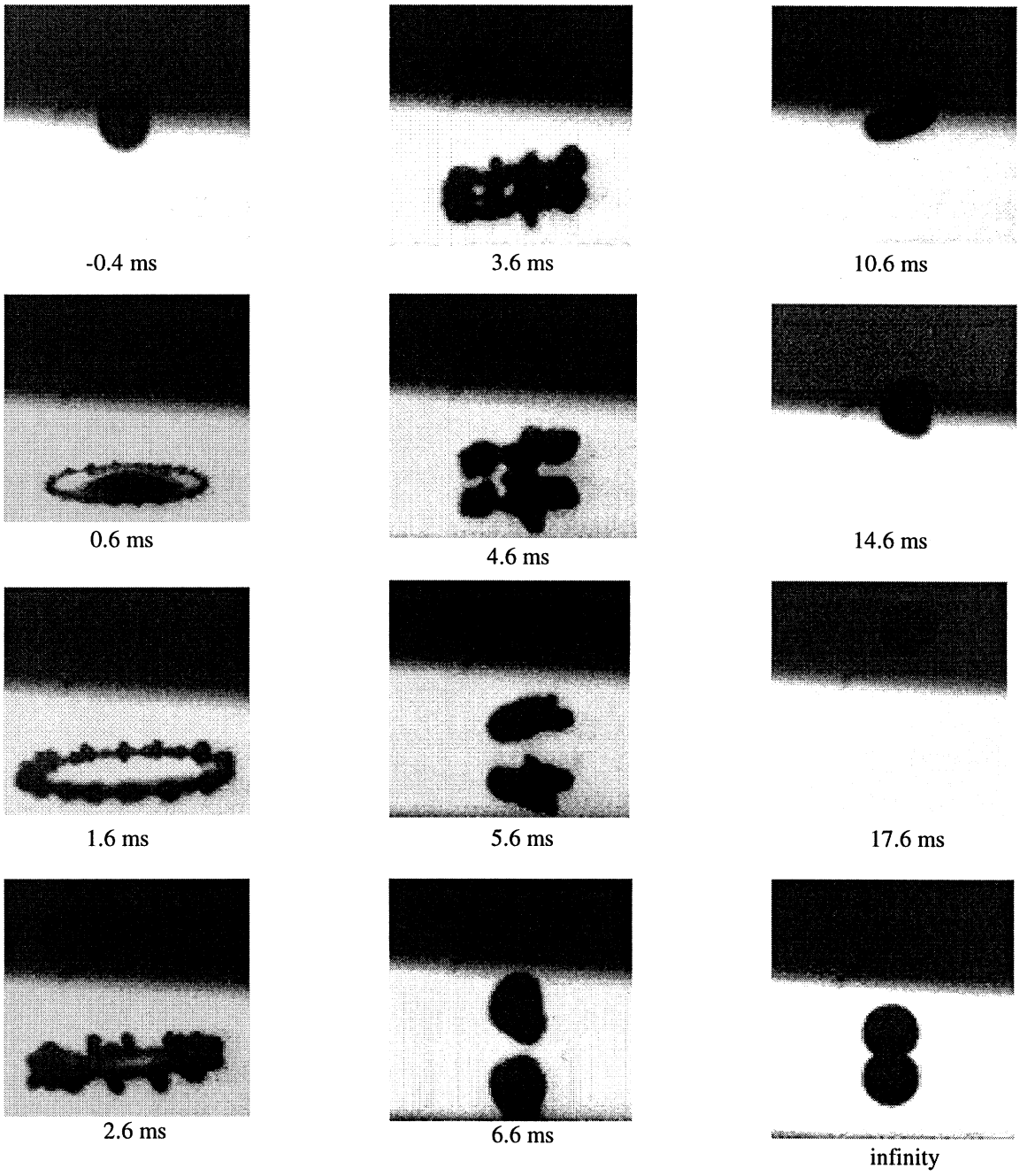
-0.4 ms
3.6 ms
10.6 ms
0.6 ms
4.6 ms
14.6 ms
1.6 ms
5.6 ms
17.6 ms
2.6 ms
6.6 ms
infinity

(b)

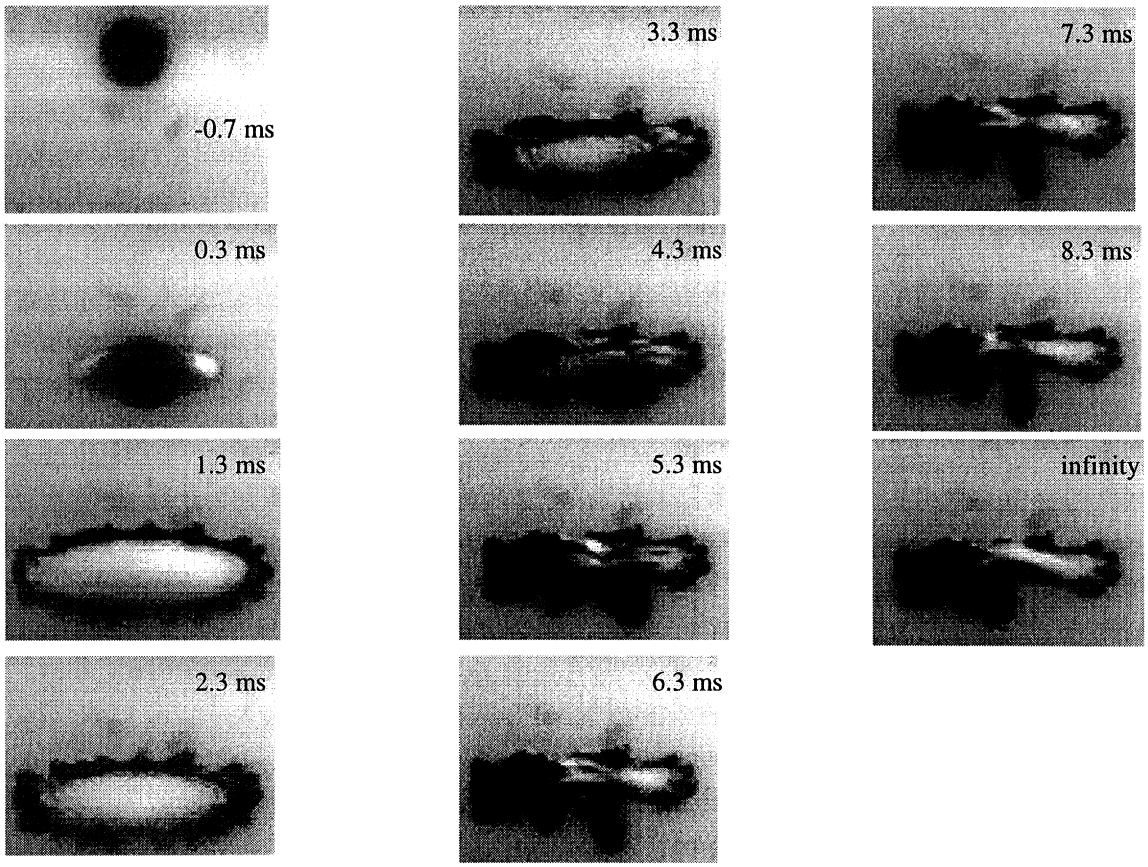

(c)

FIGURE 4.3. (a) Images of molten tin droplets arrested by solidification upon colliding with the aluminum 6061 surface. Original droplet diameter = 1.57 mm, Impact velocity = 3.04 m/s, Droplet temperature at impact = 261°C, Target temperature = 30°C. (b) Images of molten tin droplets bouncing off the stainless steel 304 surface. Original droplet diameter = 1.67 mm, Impact velocity = 3.08 m/s, Droplet temperature at impact = 263°C, Target temperature = 195°C. (c) Images of molten tin droplets colliding with the stainless steel 304 surface, showing the transitional behavior. Original droplet diameter = 1.40 mm, Impact velocity = 2.91 m/s, Droplet temperature at impact = 257°C, Target temperature = 183°C.

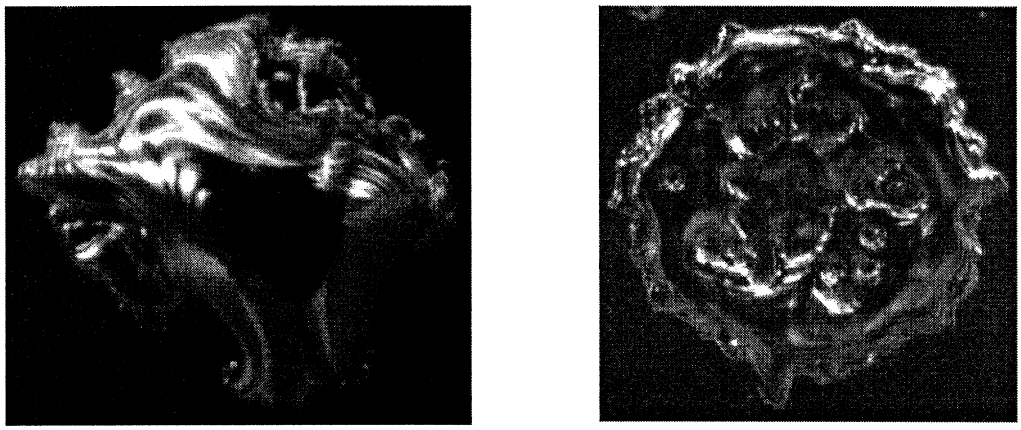

(a) (b)

FIGURE 4.4. Micro tin droplets deposited on stainless steel targets. (a) Original droplet diameter = 200 μm. (b) Original droplet diameter = 500 μm.

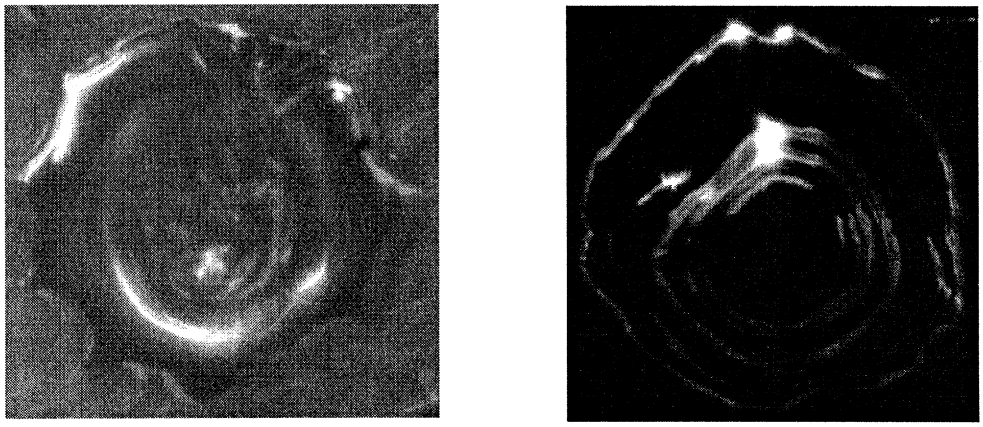

(a) (b)

FIGURE 4.5. Micro tin droplets deposited on solid tin targets. The original diameter of both the droplets is 180 μm. (a) Target temperature = 30°C. (b) Target temperature = 150°C.

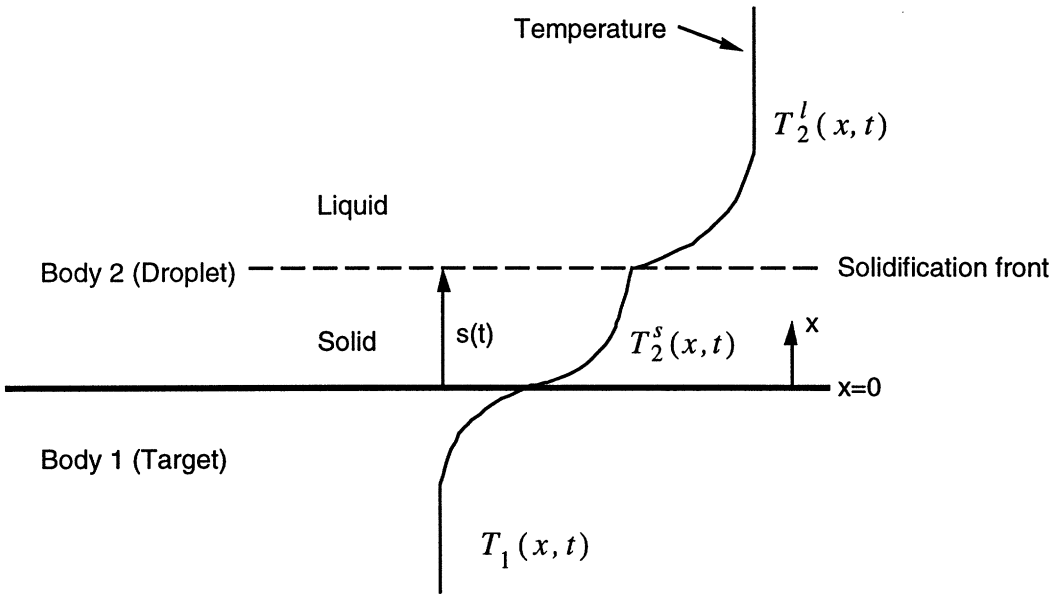

FIGURE 4.6. Geometry and temperature profile of the solidification model.

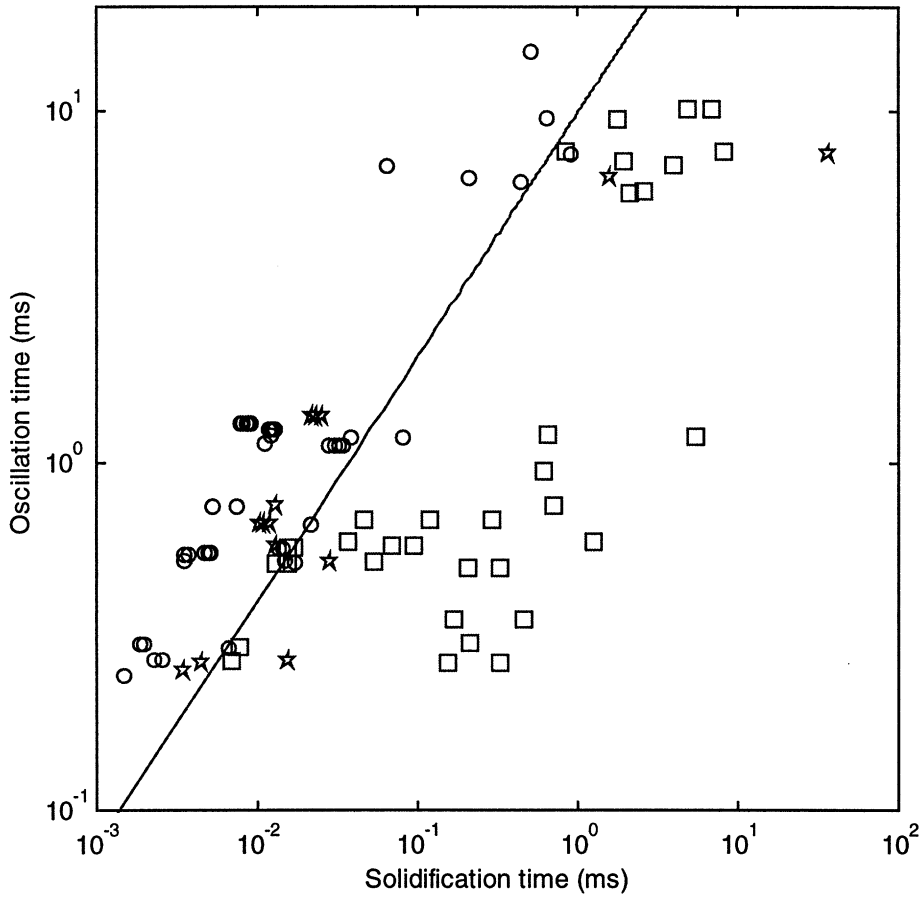

FIGURE 4.7. Regime map of bouncing and sticking for molten tin droplets. Squares and circles denote bouncing and sticking, respectively, of tin droplets on nonwetting surfaces. Pentagrams denote tin droplets deposited on the solid tin, which always stick to the target.

CHAPTER 5

CONCLUSIONS

This thesis has investigated the fundamental behavior of liquid and molten metal droplets upon collision with solid surfaces. Specifically, we have examined the physics behind splashing, post-impact oscillations, and bouncing. The studies on these phenomena expand our knowledge of the spreading behavior of liquid and molten droplets. In addition, the results obtained in this work contribute to the identification of the optimal process conditions for the droplet-based manufacturing process.

We first examined the fundamental mechanism that induces the splashing of liquid droplets. In chapter 2, we developed a linear perturbation theory of interface instabilities of a radially-expanding, liquid sheet in cylindrical geometries. The theory was applied to the expanding sheet under a spreading droplet to elucidate the origin of splashing. The base flow solutions were estimated by using mass conservation. It was shown that significant deceleration occurs in the early stages of spreading, which triggers the Rayleigh-Taylor instability. The model supposes that the main factor inducing the deceleration is not viscosity but the continuity of flow around the impact region. The theory was able to predict the most rapidly growing mode of azimuthal disturbance and its growth rate at each instant during spreading. It was found that the mode number of maximum instability changes because of time-dependent coefficients in the amplitude equation. We examined the effects of several parameters on the analysis results, including the transient profile of an interface radius, i.e., the coefficient A, the perturbation onset time t_i, and the Weber number. It was shown that larger impact inertia associated with a higher We, and thus presumably higher A, promotes interface instability and prefers higher wave number for maximum instability.

Chapter 3 investigated the oscillations of liquid droplets upon collision with solid surfaces. Our experiments showed that the droplets with high impact inertia, associated with high We and Re, more vigorously oscillate upon collision with the solid surface. The oscillation is greatly affected by the wetting between the liquid droplet and the solid surface. Good wetting weakened and slowed down the recoiling process. Moreover, experiments using droplets of different liquids and the same target solid showed the strong effects of liquid properties and wetting behavior on the oscillation phenomenon. We developed a model based on the variational principle, assuming the droplet shape as a cylinder. We also made modifications to the already existing variational model which

assumed the droplet shape as a truncated sphere. Modeling results were in good agreement with experimental data, showing the capability of our models to predict the complicated phenomena of droplet spreading and recoiling. In addition, the individual effects of parameters such as We, Re, and the contact angle, were examined. The analysis showed that the relative magnitudes of surface energy and viscous dissipation play critical roles in determining droplet dynamics. It was also shown that droplet dynamics are strongly affected by the contact angle, e.g., poor wetting greatly promotes recoiling. A significant computational effort was saved by solving a single second order, nonlinear differential equation instead of solving the full Navier-Stokes equation with the moving boundary. Furthermore, our current study showed that use of the equilibrium contact angle yields a prediction sufficiently close to the experimental measurements.

Chapter 4 studied the bouncing of the molten metal droplets upon collision with subcooled target surfaces. Experiments were performed with various conditions to obtain a fundamental understanding of the bouncing and sticking of molten droplets. We interpreted the experimental data based on the following assumption: whether the droplet will bounce or stick is determined by the competition between the relative magnitudes of the oscillation and solidification times. An empirical regime map was constructed based on these two time scales. We found a clear trend that bouncing occurs when solidification is slow compared to oscillation, while sticking is observed when the solidification is fast. Our experimental data suggest that there exist a threshold which determines whether a droplet will bounce or stick. We also found that the bouncing is prohibited by good wetting between the droplet and target, which suggests that wetting has a measurable effect on bouncing behavior.

Based on the results of this study summarized in Table 5.1, one can determine the process conditions required to obtain the desired deposition. Table 5.1 describes the effects of each nondimensional parameter on the dynamics of droplet spreading. For example, in order to get nicely spread droplets, high degree of spreading but low degree of splashing, oscillation, and bouncing are desired. Therefore, it is necessary to keep t_{osc}/t_{sol} small and • high. However, the Weber and Reynolds numbers should be optimized both to increase the spread factor and to minimize splashing and oscillation. The analytical methods in Chapter 2 and 3 select the optimal We and Re.

In conclusion, the spreading behavior of molten metal droplets in the inviscid, inertia-driven impact regime are best explained by examining the effects of factors such as We, Re, and contact angle. To determine the optimal process conditions for the droplet-based manufacturing processes, it is necessary to understand the physical mechanisms that lead to abnormal impact behavior such as splashing and bouncing. This

thesis offers physical models and experimental data to better control and prevent such phenomena.

TABLE 5.1 Effects of nondimensional parameters on the dynamics of droplet spreading. The trends in droplet spreading are described as the values of the parameters increase.

Parameter	Degree of spreading	Degree of splashing	Degree of oscillation	Degree of bouncing
We	Increase	Increase	Increase	Increase
Re	Increase	Increase	Increase	Increase
θ			Increase	Increase
t_{osc}/t_{sol}			Decrease	Decrease

BIBLIOGRAPHY

Allen, R. F., 1975, "The role of surface tension in splashing," *Journal of Colloid and Interface Science*, vol. 51, p. 350.

Baker, G. R., Meiron, D. I., and Orszag, S. A., 1984, "Boundary integral methods for axisymmetric and three-dimensional Rayleigh-Taylor instability problems," *Physica D*, vol. 12, p. 19.

Batchelor, G. K., 1967, *An Introduction to Fluid Dynamics*, Cambridge University Press, Cambridge, England.

Bechtel, S. E., Bogy, D. B., and Talke, F. E., "Impact of liquid drop against a flat surface," 1981, *IBM Journal of Research and Development*, vol. 25, p. 963.

Bennett, T. and Poulikakos, D., 1993, "Splat-quench solidification: estimating the maximum spreading of a droplet impacting a solid surface," *Journal of Materials Science*, vol. 28, p. 963.

Berning, M. and Rubenchik, A. M., 1998, "A weakly nonlinear theory for the dynamical Rayleigh-Taylor instability," *Physics of Fluids*, vol. 10, p. 1564.

Birkhoff, G., 1956, "Stability of spherical bubbles," *Quarterly of Applied Mathematics*, vol. 13, p. 451.

Bowden, F. P. and Field, J. E. 1964, "The brittle fracture of solids by liquid impact, by solid impact, and by shock," *Proceedings of the Royal Society of London, A*, vol. 282, p. 331.

Brenner, M. P., Lohse, D., and Dupont, T. F., 1995, "Bubble shape oscillations and the onset of sonoluminescence," *Physical Review Letters*, vol. 75, p. 954.

Carslaw, H. S. and Jaeger, J. C., 1959, *Conduction of Heat in Solids*, 2nd Ed., Oxford University Press, Oxford, England.

Chandra, S. and Avedisian, C. T., 1991, "On the collision of a droplet with a solid surface," *Proceedings of the Royal Society of London, A*, vol. 432, p. 13.

Chandrasekhar, S., 1961, *Hydrodynamic and Hydromagnetic Stability*, Oxford University Press, Oxford, England.

Crandall, S. H., Karnopp, D. C., Kurtz, Jr., E. F., and Pridmore-Brown, D. C., 1968, *Dynamics of Mechanical and Electromechanical Systems*, Robert E. Krieger Publishing Co., Marlbar, FL.

de Gennes, P. G., 1985, "Wetting: statics and dynamics," *Review of Modern Physics*, vol. 57, p. 827.

Engel, O. G., 1955, "Waterdrop collisions with solid surfaces," *Journal of Research of the National Bureau of Standards*, vol. 54, p. 281.

Feng, Z. C. and Leal, L. G., 1997, "Nonlinear bubble dynamics," *Annual Review of Fluid Mechanics*, vol. 29, p. 201.

Fukai, J., Shilba, Y., Yamamoto, T., Miyatake, O., Poulikakos, D. , Megaridis, C. M., and Zhao, Z., 1995, "Wetting effects on the spreading of a liquid droplet colliding with a flat surface: experiment and modeling," *Physics of Fluids*, vol. 7, p. 236.

Harlow, F. H. and Shannon, J. P., 1967, "The splash of a liquid drop," *Journal of Applied Physics*, vol. 38, p. 3855.

Hildebrand, F. B., 1976, *Advanced Calculus for Applications*, 2nd Ed., Prentice-Hall, Englewood Cliffs, NJ.

Hilgenfeldt, S., Brenner, M. P., Grossmann, S., and Lohse, D., 1998, "Analysis of Rayleigh-Plesset dynamics for sonoluminescing bubbles," *Journal of Fluid Mechanics*, vol. 365, p. 171.

Inada, S., 1988, "Transient heat transfer from a free-falling molten drop of lead to a cold plate," *Journal of Chemical Engineering of Japan*, vol. 21, p. 583.

Inada, S. and Yang, W.-J., 1994, "Solidification of molten metal droplets impinging on a cold surface," *Experimental Heat Transfer*, vol. 7, p. 93.

Kendall, G. E. and Rohsenow, W. M., 1978, "Heat transfer to impacting drops and post critical heat flux dispersed flow," Technical Report No. 85694-100, Department of Mechanical Engineering, Massachusetts Institute of Technology, Cambridge, MA.

Levin, Z. and Hobbs, P. V., 1971, "Splashing of water drops on solid and wetted surfaces: hydrodynamic and charge separation," *Philosophical Transactions of the Royal Society of London, A*, vol. 269, p. 555.

Liu, H., Lavernia, E. J., Rangel, R. H., 1993, "Numerical simulation of substrate impact and freezing of droplets in plasma spray processes," *Journal of Physics, D*, vol. 26, p. 1900.

Liu, H., Lavernia, E. J., Rangel, R. H., 1994, "Numerical investigation of micropore formation during substrate impact of molten droplets in plasma spray processes," *Atomization and Sprays*, vol. 4, p. 369.

Liu, H., Lavernia, E. J., Rangel, R. H., 1995, "Modeling of molten droplet impingement on a non-flat surface," *Acta Metallurgica et Materialia*, vol. 43, p. 2053.

Madejski, J., 1976, "Solidification of droplets on a cold surface," *International Journal of Heat and Mass Transfer*, vol. 19, p. 1009.

Marmanis, H. and Thoroddsen, S. T., 1996, "Scaling of the fingering pattern of an impacting drop," *Physics of Fluids*, vol. 8, p. 1344.

Matson, D. M., Rolland, M., and Flemings, M. C., 1998, *Solidification 1998*, edited by Marsh S.P., Dantzig, J. A., Trivedi, R., Hofmeister, W., Chu, M. G., Lavernia, E. J., and Chun, J.-H., The Minerals, Metals, & Materials Society, p. 389.

McPherson, R., 1981, "The relationship between the mechanism of formation, microstructure and properties of plasma-sprayed coatings," *Thin Solid Films*, vol. 83, p. 297.

Menikoff, R., Mjolsness, R. C., Sharp, D. H., Zemach, C., and Doyle, B. J., 1978, "Initial value problem for Rayleigh-Taylor instability of viscous fluids," *Physics of Fluids*, vol. 21, p. 1674.

Mundo, CHR., Sommerfield, M., and Tropea, C., 1995, "Droplet-wall collisions: experimental studies of the deformation and breakup process," *International Journal of Multiphase Flow*, vol. 21, p. 151.

Nakamura, S., 1991, *Applied Numerical Methods with Software*, Prentice-Hall, Englewood Cliffs, NJ.

Pasandideh-Fard, M., Qiao, S., Chandra, S., and Mostaghimi, J., 1996, "Capillary effects during droplet impact on a solid surface," *Physics of Fluids*, vol. 8, p. 650.

Pasandideh-Fard, M., Bhola, R., Chandra, S., and Mostaghimi, J., 1998, "Deposition of tin droplets on a steel plate: simulations and experiments," *International Journal of Heat and Mass Transfer*, vol. 41, p. 2929.

Plesset, M. S., 1954, "On the stability of fluid flows with spherical symmetry," *Journal of Applied Physics*, vol. 25, p. 96.

Plesset, M. S. and Mitchell, T. P., 1956, "On the stability of the spherical shape of a vapor cavity in a liquid," *Quarterly of Applied Mathematics*, vol. 13, p. 419.

Plesset, M. S. and Prosperetti, A., 1977, "Bubble Dynamics and Cavitation," *Annual Review of Fluid Mechanics*, vol. 9, p. 145.

Rayleigh, Lord, 1879, "On the capillary phenomena of jets," *Proceedings of the Royal Society of London,* vol. 29, p. 71.

San Marchi, C., Liu, H., Lavernia, E. J., Rangel, R. H., Sickinger, A., and Muehlberger, E., 1993, "Numerical analysis of the deformation and solidification of a single droplet impinging onto a flat substrate," *Journal of Materials Science*, vol. 28, p. 3313.

Schiaffino, S., 1996, "The fundamentals of molten microdrop deposition and solidification," Ph.D. thesis, Department of Mechanical Engineering, Massachusetts Institute of Technology, Cambridge, MA.

Schiaffino, S. and Sonin, A. A., 1997, "Molten droplet deposition and solidification at low Weber numbers," *Physics of Fluids*, vol. 9, p. 3172.

Shi, H.-H. and Dear, J. P., 1992, "Oblique high-speed liquid-solid impact," *JSME International Journal, I*, vol. 35, p. 285.

Solonenko, O. P., Ushio, M., and Ohmori, A., 1994, "The complex study of "metal drop-substrate" interaction," *Proceedings of International Seminar ISECTA '93*, Almaty, Kazakhstan, p. 319.

Stow, C. D. and Hadfield, M. G., 1981, "An experimental investigation of fluid flow resulting from the impact of a water drop with an unyielding dry surface," *Proceedings of the Royal Society of London, A,* vol. 373, p. 419.

Taylor, G. I., 1950, "The instability of liquid surfaces when accelerated in a direction perpendicular to their planes. I," *Proceedings of the Royal Society of London, A*, vol. 201, p. 192.

Thoroddsen, S. T., and Sakakibara, J., 1998, "Evolution of the fingering pattern of an impacting drop," *Physics of Fluids*, vol. 10, p. 1359.

Trapaga, G. and Szekely, J. 1991, "Mathematical modeling of the isothermal impingement of liquid droplets in spraying processes," *Metallurgical Transactions, B*, vol. 22B, p. 901.

Trapaga, G., Matthys, E. F., Valencia, J. J., and Szekely, J., 1992, "Fluid flow, heat transfer, and solidification of molten metal droplets impinging on substrates: comparison of numerical and experimental results," *Metallurgical Transactions, B*, vol. 23B, p. 701.

Tryggvason, G., 1988, "Numerical simulations of the Rayleigh-Taylor instability," *Journal of Computational Physics*, vol. 75, p. 253.

Tsurutani, K., Yao, M., Senda, J., and Fujimoto, H., 1990, "Numerical analysis of the deformation process of a droplet impinging upon a wall," *JSME International Journal, II*, vol. 33, p. 555.

Waldvogel, J. M. and Poulikakos, D., 1997, "Solidification phenomena in picoliter size solder droplet deposition on a composite substrate," *International Journal of Heat and Mass Transfer*, vol. 40, p. 295.

Watanabe, T., Kuribayashi, I., Honda, T., and Kanzawa, A., 1992, "Deformation and solidification of a droplet on a cold substrate," *Chemical Engineering Science*, vol. 47, p. 3059.

Wilkes, E. D. and Basaran, O. A., "Forced oscillations of pendant (sessile) drops," 1997, *Physics of Fluids*, vol. 9, pp. 1512.

Worthington, A. M., 1877a, "On the forms assumed by drops of liquid falling on a horizontal plate," *Proceedings of the Royal Society of London*, vol. 25, p. 261.

Worthington, A. M., 1877b, "A second paper on the forms assumed by drops of liquid falling on a horizontal plate," *Proceedings of the Royal Society of London*, vol. 25, p. 498.

Xiong, B., Megaridis, C. M., Poulikakos, D., Hoang, H., 1998, "An investigation of key factors affecting solder microdroplet deposition," *Journal of Heat Transfer*, vol. 120, p. 259.

Yim, P., Chun, J.-H., Ando, T., and Sikka, V. K., 1996, "Production and characterization of mono-sized Sn-Pb alloy balls," *International Journal of Powder Metallurgy*, vol. 32, p. 155.

Zhang, X. and Basaran, O. A., 1997, "Dynamic surface tension effects in impact of a drop with a solid surface," *Journal of Colloid and Interface Science*, vol. 187, p. 166.

APPENDICES

APPENDIX A. NONDIMENSIONAL QUANTITIES OF CHAPTER 2

The following gives the definitions of the nondimensional quantities used in Chapter 2. Note that all the asterisked symbols denote dimensional quantities, whereas non-asterisked symbols are the corresponding nondimensional quantities.

$$A_m = \frac{A_m^* R_D^{*(m-1)}}{U^*}$$

$$f_m = \frac{f_m^*}{R_D^*}$$

$$M = \frac{M^*}{R_D^* U^*}$$

$$r = \frac{r^*}{R_D^*}$$

$$R = \frac{R^*}{R_D^*}$$

$$R_i = \frac{R_i^*}{R_D^*} \qquad (i = 0, 1)$$

$$v_r = \frac{v_r^*}{U^*}$$

$$v_\theta = \frac{v_\theta^*}{U^*}$$

$$t = \frac{t^*}{\tau^*}$$

$$\Delta P_0 = \frac{\Delta P_0^*}{\rho^* U^{*2}}$$

$$\phi = \frac{\phi^*}{R_D^* U^*}$$

$$\phi_i = \frac{\phi_i^*}{R_D^* U^*} \qquad (i = 0, 1)$$

$$\kappa = \kappa^* R_D^*$$

APPENDIX B. FREQUENCY OF PERTURBATIONS TO A CONSTANT RADIUS LIQUID SHEET

In Chandrasekhar (1961), the frequency for the mth mode azimuthal perturbation on a columnar liquid jet ω_m is given by, in the present nondimensionalization,

$$\omega_m^2 = \frac{1}{R_0^3 \mathrm{We}} \frac{x I_m'(x)}{I_m(x)} \left(m^2 + x^2 - 1\right), \tag{B1}$$

where $x = kR_0$, k denoting the wave number in z-direction, and I_m is the modified Bessel function of the first kind, of order m. We show that for a two dimensional liquid sheet whose unperturbed radius R_0 is kept unity, Eq. (B1) is reduced to Eq. (26). Using the following identities (Hildebrand 1976):

$$I_m'(k) = I_{m+1}(k) + \frac{m}{k} I_m(k), \tag{B2}$$

$$I_m(k) = \sum_{j=0}^{\infty} \frac{(k/2)^{2j+m}}{j!(j+m)!}, \tag{B3}$$

we find

$$\lim_{k \to 0} \frac{k I_m'(k)}{I_m(k)} = m. \tag{B4}$$

Therefore, in the limit $k \to 0$, Eq. (B1) is identical to Eq. (26).

APPENDIX C. EXPERIMENTAL EVIDENCE OF CHAPTER 2

Figure C.1 shows a splat of a pure tin droplet deposited on a 304 stainless steel surface polished with the 1-μm diamond paste. Figure C.1 (b) clearly shows the development of fingers owing to the rapid freezing of the droplet bottom. It shows that the fingers, which remain until the spreading stops, have in fact been generated immediately after the impact. Therefore, one can conclude that the behavior of the spreading front near the moment of impact is critical in understanding the splashing phenomenon.

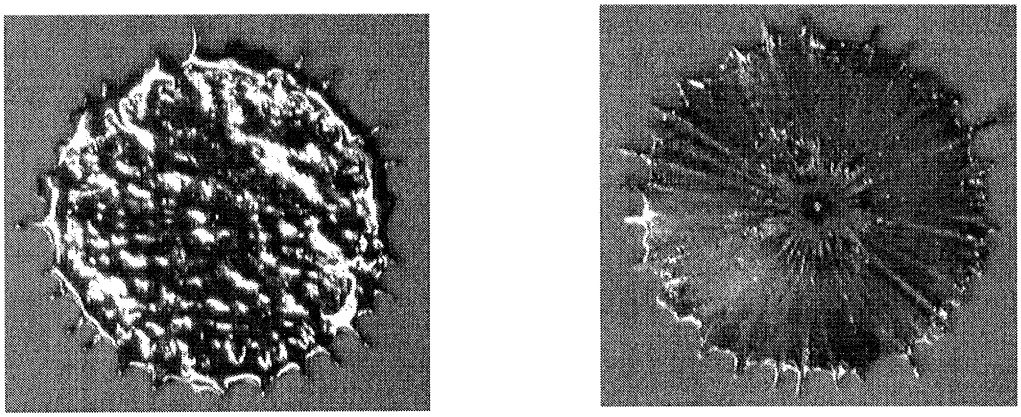

(a) (b)

FIGURE C.1. Splashed tin splat. (a) Top of the splat. (b) Bottom of the splat. The impact conditions: impact velocity = 3.5 m/s, initial droplet diameter = 2.6 mm, droplet temperature at impact = 315°C, target temperature = 30°C, We = 203, and Re = 17100.

APPENDIX D. NONDIMENSIONAL QUANTITIES OF CHAPTER 3

The following gives the definitions of the nondimensional quantities used in Chapter 3. Note that all the asterisked symbols denote dimensional quantities, whereas non-asterisked symbols are the corresponding nondimensional quantities.

$$D_b = \frac{D_b^*}{D^*}$$

$$h = \frac{h^*}{D^*}$$

$$r = \frac{r^*}{D^*}$$

$$t = \frac{t^*}{\left(\rho^* D^* / \sigma^*\right)^{1/2}}$$

$$T = \frac{T^*}{\pi \rho^* D^{*3} U^{*2} / 12}$$

$$v_z = \frac{v_z^*}{U^*}$$

$$v_r = \frac{v_r^*}{U^*}$$

$$V = \frac{V^*}{\pi \rho^* D^{*3} U^{*2} / 12}$$

$$Vol = \frac{Vol^*}{\pi D^{*3} / 6}$$

$$W_f = \frac{W_f^*}{\pi \rho^* D^{*3} U^{*2} / 12}$$

$$\tau = \frac{\tau^*}{\mu^* U^* / D^*}$$

APPENDIX E. MEASUREMENT OF EQUILIBRIUM CONTACT ANGLES

We use the sessile drop method to measure the equilibrium contact angles between various liquids and solids. In this method, the contact angle of a small droplet placed on a solid surface is deduced by measuring the base diameter and the height of the sessile drop. Assuming that the sessile droplet takes a shape of a spherical cap, as shown in Figure E.1, we obtain the following relation between the contact angle θ and the height h and the base diameter D_b of the droplet:

$$\theta = \sin^{-1}\left[\frac{hD_b}{\left(h^2 + D_b^2/4\right)}\right] \text{ when } \theta < \pi/2. \tag{E.1}$$

To take into account a slight deformation of the sessile droplet of a finite volume due to gravity, measurements are made with droplets of decreasing volumes. The equilibrium value is obtained by extrapolating the data to zero volume (Schiaffino 1996). The volume of the droplet V_d is given by

$$V_d = \frac{\pi}{24}\frac{(1-\cos\theta)(2+\cos\theta)}{\sin\theta(1+\cos\theta)}D_b^3 \text{ when } \theta < \pi/2. \tag{E.2}$$

Table E.1 presents the measurement results.

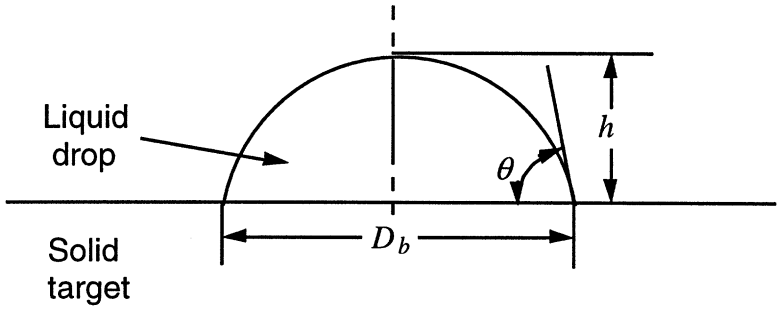

FIGURE E.1. Geometry of a sessile droplet of the spherical cap shape.

TABLE E.1. Equilibrium contact angles.

Liquid	Solid	Contact angle
Deionized water	Acrylic	87.4°
Deionized water	Silicon oxide	58.6°
Ink	Acrylic	70.9°
Ink	Silicon oxide	51.5°
Silicone oil	Acrylic	6.2°